

## **Antimony-modified soda-lime-silica glass: towards low-cost radiation-resistant materials**

GUPTA, Gaurav <<http://orcid.org/0000-0002-2948-6740>>, CHEN, Tzu-Yu, RAUTIYAL, Prince, WILLIAMS, A, JOHNSON, J, JOHNSON, C, EDGE, Ruth and BINGHAM, Paul <<http://orcid.org/0000-0001-6017-0798>>

Available from Sheffield Hallam University Research Archive (SHURA) at:

<https://shura.shu.ac.uk/29846/>

---

This document is the Accepted Version [AM]

### **Citation:**

GUPTA, Gaurav, CHEN, Tzu-Yu, RAUTIYAL, Prince, WILLIAMS, A, JOHNSON, J, JOHNSON, C, EDGE, Ruth and BINGHAM, Paul (2022). Antimony-modified soda-lime-silica glass: towards low-cost radiation-resistant materials. *Journal of Non-Crystalline Solids*, 585, p. 121526. [Article]

---

### **Copyright and re-use policy**

See <http://shura.shu.ac.uk/information.html>

# Antimony-modified soda-lime-silica glass: towards low-cost radiation-resistant materials

G. Gupta<sup>1</sup>, T.-Y. Chen<sup>1</sup>, P. Rautiyal<sup>1</sup>, A. G. Williams<sup>2</sup>, J. A. Johnson<sup>2</sup>, C. E. Johnson<sup>2</sup>, R. Edge<sup>3</sup>, P. A. Bingham<sup>1,\*</sup>

<sup>1</sup>*Materials and Engineering Research Institute, College of Business, Technology and Engineering, Sheffield Hallam University, City Campus, Howard Street, Sheffield, S1 1WB, UK*

<sup>2</sup>*Department of Mechanical, Aerospace and Biomedical Engineering, University of Tennessee Space Institute, Tullahoma, TN 37388, USA*

<sup>3</sup>*The School of Mechanical, Aerospace and Civil Engineering, University of Manchester, Oxford Road, Manchester, M19 9PL, UK*

\*Corresponding Author email: [p.a.bingham@shu.ac.uk](mailto:p.a.bingham@shu.ac.uk)

## Abstract

The development of inexpensive radiation-resistant glass is important for potential applications in displays, optics, and nuclear or space environments. This study considers the  $\gamma$ -ray and X-ray resistance of glasses relevant to low-cost float glass (i.e.,  $\text{SiO}_2\text{-Na}_2\text{O-CaO-MgO}$ ), modified with various concentrations (0 – 10 mol%) of  $\text{Sb}_2\text{O}_3$ . Various doses (0, 0.2, 2.0, and 5.0 MGy) of  $\gamma$ -rays from the decay of  $^{60}\text{Co}$  nuclei, and X-rays generated by an X-ray fluorescence (XRF) spectrometer, have been applied to this series of  $\text{Sb}_2\text{O}_3$ -modified float-type glasses to study their resistance to radiation-induced damage. Irradiation leads to the formation of various defect centres ( $\text{HC}_2$ ,  $\text{HC}_1$ ,  $\text{TE}$ ,  $\text{E}'$ , and  $\text{E}^-$  types). These radiation-induced defects cause photo-darkening of the glass, which reduces its visible-wavelength optical transparency. The addition of  $\text{Sb}_2\text{O}_3$  to these glasses led to reductions in the formation of radiation-induced defect-centres, combined with forbidden bandgap narrowing which led to non-linear changes in visible-wavelength absorption as a function of  $\text{Sb}_2\text{O}_3$  content such that

26 the most transparent irradiated glasses were advantageously obtained at low (0.5 mol%)  
27  $\text{Sb}_2\text{O}_3$  content. The mechanisms of defect-formation involve the creation of  $\text{Sb}^{4+}$ -ions which  
28 assists in mitigating the effects of irradiation on the visible-wavelength transparency of the  
29 glass. The 0.5 mol% of  $\text{Sb}_2\text{O}_3$ -modified float glass provided a maximized concentration of  
30  $\text{Sb}^{4+}$ -ions upon  $\gamma$ -ray irradiation. Combined with the smallest changes in the UV band gap  
31 narrowing, it enabled this glass to retain the highest visible-wavelength transparency at all  
32 doses of ionizing radiation studied (0.2, 2 and 5 MGy). This work confirms the substantially  
33 enhanced radiation resistance of  $\text{Sb}_2\text{O}_3$ -modified float-type glasses compared to standard  
34 float glass, which could potentially be further developed towards commercialization, for  
35 example as a low-cost solution for radiation resistant applications.

36

## 37 **1. Introduction**

38 Photo-darkening of commercial glass systems interacting with ionizing radiation has  
39 been previously studied across a range of systems and scenarios [1–10]. Both UV-Vis-NIR  
40 optical absorption spectroscopy and electron paramagnetic resonance (EPR) techniques have  
41 been employed to better understand radiation-induced effects in glass systems [1–10]. Based  
42 on these and other articles, two interesting conclusions may be drawn regarding the  
43 mechanisms involved:

- 44 I. Trapping of electrons in defects existing before glass irradiation; or
- 45 II. Defect centres created during the irradiation process

46 The radiation-induced defects in the amorphous form of  $\text{SiO}_2$  (a- $\text{SiO}_2$ ) and silica based  
47 glass have been studied in depth by various research groups [1,3,10–14]. Electron  
48 Paramagnetic Resonance (EPR) studies have confirmed the formation of paramagnetic  
49 radiation-induced defects [11]. EPR studies reveal that the fundamental radiation-induced

50 defect centres in silica systems are  $E'$ -centres [15], non-bridging-oxygen hole centres  
 51 (NBOHC) [16], peroxy-radicals (POR) [17] and self-trapped holes (STH) [18]. The radiolytic  
 52 process of formation of  $E'$ -centres can be presented as  $[\equiv\text{Si}:\text{Si}\equiv]^0 + h^+ \rightarrow [\equiv\text{Si}\cdot + \text{Si}\equiv]^+$ , where  
 53 ‘ $\equiv$ ’ represents the bonds to 3 bridging oxygens in the glass network, ‘ $\cdot$ ’ represents a pair of  
 54 electrons equally shared between two adjacent silicon atoms, the ‘ $\cdot$ ’ implies an unpaired  
 55 electron localized in a dangling  $sp^3$  orbital of a single silicon atom, and ‘ $h^+$ ’ defines the hole  
 56 interacting with the glass network [19]. The fission of strained Si-O-Si bonds causes the  
 57 formation of NBOHC (i.e.,  $\equiv\text{Si}-\text{O}\cdot$ ) defects [11]. The peroxy-radicals (POR, i.e.,  $\equiv\text{Si}-\text{O}-\text{O}\cdot$ )  
 58 are formed via several pathways [11,19]. Self-trapped holes are of two types:  $\text{STH}_1$  contains a  
 59 hole trapped in a bridging oxygen network (i.e.,  $\equiv\text{Si}-\dot{\text{O}}-\text{Si}\equiv$ ), while  $\text{STH}_2$  comprises a hole  
 60 delocalized over two bridging oxygens [11,12]. In general, all of the stable paramagnetic  
 61 defects have half-filled energy levels located in the optical band gap, hence such defects give  
 62 rise to optical absorption bands [11].

63 These radiation-induced defects trap the electrons that give rise to so-called “colour  
 64 centres” [1–3,10,11,19–22]. The absorption peak position and relative intensity of the various  
 65 colour centres within irradiated soda-lime-silica glasses varies with glass-melting  
 66 environment (oxidizing or reducing) [1]. Ionizing radiation-induced absorption bands are  
 67 reported at (a) 590 – 620 nm (i.e., 16,949 - 16,129  $\text{cm}^{-1}$  or 2.0 – 2.1 eV), (b) 430 – 450 nm  
 68 (i.e., 23,256 - 22,222  $\text{cm}^{-1}$  or 2.75 – 2.90 eV), (c) 300 – 310 nm (i.e., 33,333 – 32,258  $\text{cm}^{-1}$  or  
 69 4.0 – 4.1 eV), and (d) 225 – 235 nm (i.e., 44,444 - 42,553  $\text{cm}^{-1}$  5.3 – 5.6 eV) for soda-lime-  
 70 silica systems [1,19,20,23]. The origin of radiation-induced absorption band near 16,500  $\text{cm}^{-1}$   
 71 (2.0 eV) has been attributed to both POR ( $\equiv\text{Si}-\text{O}-\text{O}\cdot$ ) and NBOHC or  $\text{HC}_2$  ( $\equiv\text{Si}-\text{O}\cdot$ ) [10,23].  
 72 According to Zatsépin *et al.* [20] and others [1, 23], the radiation-induced absorption band at  
 73 around 22,200  $\text{cm}^{-1}$  (2.75 eV) is manifested for  $\text{Na}_2\text{O}$  or  $\text{K}_2\text{O}$  modified silica glasses  
 74 [1,20,23]. This band has been attributed to modified NBOHC-centres (i.e.,  $\text{HC}_1 \rightarrow \equiv\text{Si}-$

75  $\dot{O}\dots\text{Me}^+$ , where ‘...’ presents the dangling bond) [20]. The absorption band near  $33,300\text{ cm}^{-1}$   
76 ( $4.0\text{ eV}$ ) has been attributed to trapped electron defects [23] and the band near  $43,500\text{ cm}^{-1}$   
77 ( $5.4\text{ eV}$ ) has been attributed to  $E'$ -centres [23].

78 Radiation-hard glasses are glasses with compositional modifications, often enabled by  
79 the incorporation of transition metals or lanthanides, that reduce defect centre related  
80 colouration effects. Ions such as  $\text{Ce}^{3+}$ ,  $\text{Fe}^{2+}$  and  $\text{Mn}^{2+}$  capture the holes, which evolve after  
81 the interaction of ionizing radiations [1,24–27]. In contrast, ions including  $\text{Ce}^{4+}$ ,  $\text{Eu}^{3+}$  and  $\text{Ti}^{4+}$   
82 capture the electrons after interaction with  $\gamma$ -rays [1,2,24,25,28,29]. Baccaro *et al.* [9]  
83 reported the effects of  $\text{Ce}^{3+}/\text{Ce}^{4+}$  ion-modified borosilicate glass for radiation-resistance over  
84 a wide range of  $\gamma$ -ray doses, with applications in radiation-resistant windows [9]. The  
85 addition to oxide glasses of  $\text{Ce}^{3+}/\text{Ce}^{4+}$  has provided radiation resistance for many years and  
86 commercially produced “*radiation-hard*” glasses typically use  $\text{Ce}^{3+}/\text{Ce}^{4+}$  ions in the network  
87 to provide resistance from extreme high-radiation environments such as in space or the  
88 nuclear industry [8,9,30,31]. Apart from cerium, only a few elements can exist in multiple  
89 oxidation states within oxide glasses whilst producing little or no visible absorption  
90 (colouration) when present at concentrations sufficient to provide significant added resistance  
91 to radiation damage ( $>\text{ca. } 1\text{ wt. } \%$ ) [9,31,32]. In oxide glass, most transition metals and  
92 lanthanides produce visible absorption bands due to  $d-d$  or  $f-f$  transitions [33–37] and  
93 substantial levels of doping would render such glasses moderately or strongly coloured,  
94 depending on the nature of the additive/s and the redox conditions associated with glass  
95 preparation. Many glass applications require high visible-range transparency so the addition  
96 of most of the transition metals and many of the lanthanides is not an option, hence the  
97 widespread use of  $\text{Ce}^{3+}/\text{Ce}^{4+}$  for radiation resistance, since neither of these oxidation states of  
98 cerium produces strong absorption bands centred at visible wavelengths. However, a number  
99 of first, second and third-row transition metals, when present in oxidation states with  $d^0$

100 configurations, produce no visible absorption bands [33–37]. A number of these have been  
101 studied for potential solar energy UV protection and downshifting applications [38,39].

102 Glasses with transition metal dopants present in their colourless oxidation states can, in  
103 some cases, develop extrinsic defects, by photo-oxidation or photo-reduction, which manifest  
104 as visible or UV absorption bands, for high-energy (UV, X-ray,  $\gamma$ -ray) and high-dose  
105 radiation [4,7,40]. Traditionally referred to as solarisation (in the context of UV from  
106 sunlight), this is a well-known phenomenon that describes radiation-induced changes in  
107 oxidation state [4,7,40–47]. For example,  $Mn^{3+}$  was used for many centuries [40,48] to  
108 decolourise glasses by oxidising  $Fe^{2+}$  to  $Fe^{3+}$  through the redox reaction  $Mn^{3+} + Fe^{2+} \rightarrow$   
109  $Mn^{2+} + Fe^{3+}$  [4,7]. However, prolonged exposure to UV radiation could supply sufficient  
110 photons with adequate energy to measurably reverse this reaction and oxidise  $Mn^{2+}$  to  $Mn^{3+}$ ,  
111 which gives rise to visible absorption bands, via the redox reaction  $Mn^{2+} + Fe^{3+} + h\nu \rightarrow$   
112  $Mn^{3+} + Fe^{2+}$  [33,40]. Photo-oxidation or photo-reduction reactions have been documented  
113 for many multivalent cations in oxide glasses – principally at low ( $\ll 1$  wt %) abundance and  
114 principally for transition metals and lanthanides [2,4,5,7–9,32,33,40,42,49–58]; but also post-  
115 transition metals (e.g. Nb, Ta, W) and the so-called heavy metals including Sb, As and Pb  
116 [6,7,42,45–47,53,59,60]. These include cations which undergo “*colourless to coloured*”  
117 photo-oxidation or photo-reduction, for example,  $Ti^{4+} \rightarrow Ti^{3+}$ ,  $Mn^{2+} \rightarrow Mn^{3+}$  or  $Nb^{5+} \rightarrow$   
118  $Nb^{4+}$ . The presence of multivalent cations including  $Fe^{2+}/Fe^{3+}$  [1,4,7,21,56,61–64],  $Ce^{3+}/Ce^{4+}$   
119 [1,4,7,52,61],  $Cu^0/Cu^+/Cu^{2+}$  [4,7,54–56],  $Mn^{2+}/Mn^{3+}$  [1,4,7,55–57,61,65],  $Ti^{3+}/Ti^{4+}$   
120 [1,2,4,7,44,46,47,52] and other transition metals, lanthanides and heavy metals  
121 [1,2,4,5,7,49,51–53,55,56,58,60,61] can have varying degrees of efficacy, depending on their  
122 abundance and distribution in the glass; the nature, energy, and dose of irradiation; the glass  
123 composition and structure; and the glass melting (redox) conditions.

124 To minimise the formation of extrinsic or intrinsic visible colour centres through photo-  
125 oxidation or photo-reduction, it is essential to avoid any multivalent constituents which  
126 produce absorption bands centred at visible wavelengths. Most multivalent ions can access  
127 various oxidation states by melting under extreme redox conditions [66,67] (e.g., sufficient to  
128 reduce cations to their metallic forms), to cause visible or near-IR (for solar energy /  
129 photovoltaic applications) absorption bands.

130 One such multivalent element, which produces no visible absorption bands in any  
131 nonzero oxidation state, is antimony. There is evidence that  $\text{Sb}_2\text{O}_3$  can render oxide glasses  
132 more resistant to the formation of radiation-induced defects [52,60,68–70], and  $\text{Sb}_2\text{O}_3$   
133 additions can provide enhanced resistance to  $\gamma$ -radiation when present with other active  
134 dopants [60,69,71]. The effect of radiation-induced attenuation has been studied for  $\text{Sb}_2\text{O}_3$   
135 and  $\text{Nb}_2\text{O}_5$  modified  $\text{P}_2\text{O}_5$ – $\text{K}_2\text{O}$ – $\text{BaO}$ – $\text{Al}_2\text{O}_3$  glass [60]. The  $\gamma$ -irradiated base glass as well as  
136  $\text{Nb}_2\text{O}_5$ -modified glasses revealed a very broad, intense absorption band centred at 330 – 700  
137 nm ( $30,300$  –  $14,300$   $\text{cm}^{-1}$ ). However, the  $\text{Sb}_2\text{O}_3$ -modified glasses did not show any  
138 additional absorption bands. EPR analysis of those  $\gamma$ -ray exposed glass samples showed two  
139 types of response [60]. The major EPR signal consisted of sharp hyperfine splitting  
140 associated with  $\text{PO}_2$ ,  $\text{PO}_3$ ,  $\text{PO}_4$ , and phosphorus-oxygen hole centres (*POHC*: an unpaired  
141 electron shared by two NBO atoms bonded with the same phosphorus) [3,60]. The minor  
142 signal had larger hyperfine splitting with broad lines, which is associated with phosphorus-  
143 oxygen electron centres (*POEC*:  $\text{PO}_2$ ,  $\text{PO}_3$ ,  $\text{PO}_4$  complexes that consist of unpaired electrons  
144 localized on the central P-atom). The base glass showed both major and minor EPR bands,  
145 under  $\gamma$ -ray exposure. However, the  $\text{Nb}_2\text{O}_5$ -modified phosphate glass exhibited only the  
146 major EPR response, while  $\text{Sb}_2\text{O}_3$ -modified samples showed both EPR bands were absent.  
147 The  $\gamma$ -ray generated electron-hole pair must therefore be retained in the phosphate base glass  
148 by redox reactions, (A)  $\text{PO} + h^+ \rightarrow \text{POHC}$  ( $h^+$ : Hole from electron-hole pair production) and

149 (B)  $PO + e^- \rightarrow POEC$  ( $e^-$ : electron from electron-hole pair production). However, the  $Nb^{5+}$   
150 ions, which act as an electron capture centre, following the redox reaction  $Nb^{5+} + e^- \rightarrow Nb^{4+}$ ,  
151 whereas some  $PO$  captures the hole in the vicinity of the  $Nb^{5+}$  ion. Further, the process of  
152 electron-capture could cause the formation of  $Nb^{4+}-O-Nb^{4+}$  or  $Nb^{4+}-O^-$  complexes and  
153 possibly lead to the formation of  $Nb^{3+}-O-Nb^{5+}$  units [71–73]. On the contrary, for  $Sb_2O_3$ -  
154 containing glasses,  $Sb^{3+}$ -ions act as a hole-trapping centre that follows the redox reaction  $Sb^{3+}$   
155  $+ h^+ \rightarrow Sb^{4+}$  [60]. The nearest  $PO$  captures the  $e^-$  to result in  $POEC$ , in this process [60].  
156 However,  $Sb^{4+}$  has instabilities at room temperature that causes a further redox reaction,  $Sb^{3+}$   
157  $+ 2Sb^{4+} \rightarrow Sb^{5+} + 2Sb^{3+}$  [60]. Now, the electrons captured in  $POEC$  must be absorbed by the  
158  $Sb^{5+}$  ions to recover  $Sb^{3+}$  by the redox reaction,  $Sb^{5+} + 2POEC \rightarrow Sb^{3+} + 2PO$  [60]. By this  
159 method, the  $Sb^{3+}$  ions are recovered in the process of  $\gamma$ -ray absorption, and the net effect on  
160 the glass system is that it remains unaltered. As a result, the EPR spectra of  $Sb_2O_3$ -modified  
161 phosphate glasses remain unaffected by  $\gamma$ -ray irradiation [60].

162 The present study investigated the radiation-resistant performance of  $Sb_2O_3$ -modified  
163 soda-lime-silica (SLS) glass, building on our previous study to characterise the base glass and  
164 Sb-doped glasses [74]. The radiation-resistant performance of various concentrations (0 – 10  
165 mol%) of  $Sb_2O_3$  modified SLS glass has been substantiated for high doses (up to  $5 \times 10^6$  Gy)  
166 of  $^{60}Co$   $\gamma$ -rays and for X-ray irradiation. The impacts of  $Sb_2O_3$  on the levels and nature of  
167 radiation-induced defects in soda-lime-silica type glasses, relevant to float glass manufacture,  
168 were here studied by UV-Vis-nIR optical absorption EPR and  $^{121}Sb$  Mössbauer  
169 spectroscopies.

170

## 171 2. Experimental Procedures

172 This study explored the radiation-induced changes in a float glass-type  $\text{SiO}_2\text{-Na}_2\text{O-}$   
173  $\text{CaO-MgO}$  glass modified with various concentrations (0.0, 0.5, 1.0, 5.0, and 10.0 mol%) of  
174  $\text{Sb}_2\text{O}_3$ . The detailed glass synthesis protocol, X-ray fluorescence (XRF) determined  
175 compositional analysis, thermal properties, and structural analysis were detailed in a previous  
176 publication [74]. The base glass (i.e., SLS glass modified with 0.0 mol% of  $\text{Sb}_2\text{O}_3$ ) in this  
177 study was labelled sample SLS. The glasses modified with  $x$  mol% of  $\text{Sb}_2\text{O}_3$  were denoted  
178  $\text{Sb}_x$ ; on this basis,  $\text{Sb0.5}$ ,  $\text{Sb1.0}$ ,  $\text{Sb5.0}$ , and  $\text{Sb10.0}$  are labelled. The undoped (SLS,  $\text{Sb}_2\text{O}_3$ -  
179 free) base glass had a nominal composition of (mol %):  $\text{SiO}_2$  70.67;  $\text{Na}_2\text{O}$  13.76;  $\text{MgO}$  5.49;  
180  $\text{CaO}$  9.27;  $\text{Al}_2\text{O}_3$  0.59;  $\text{SO}_3$  0.22. Full and detailed analysis and discussion of this series of  
181 glasses can be found in [74].

182 To study their radiation behaviour, glass samples were irradiated with  $\gamma$ -rays and X-  
183 rays. The  $\gamma$ -ray irradiation experiments were executed employing a Foss Therapy Services  
184 812, equipped with a  $^{60}\text{Co}$  gamma irradiator at the Dalton Cumbrian Facility at The  
185 University of Manchester, which provides gamma photons with energies of 1.17 – 1.33 MeV  
186 [75]. In this study, glasses were irradiated with doses of 0.2, 2.0, and 5.0 MGy of  $\gamma$ -rays. The  
187 experimental conditions for the  $\gamma$ -irradiation were similar to one of our previous studies [76]  
188 to enable a consistent approach. A wavelength dispersive Philips PW2440 sequential X-ray  
189 fluorescence spectrometer (XRF) was employed as the source for X-ray irradiation. The XRF  
190 tube is a source of continuous X-rays, delivering photon energies from 0.2 keV to 35.5 keV.

191 Glasses were analysed using UV-Vis-nIR absorption spectroscopy and X-band electron  
192 paramagnetic resonance (EPR) spectroscopic techniques. UV-Vis-nIR absorption spectra  
193 were collected from flat and optically polished sample at room temperature, using a Varian  
194 Cary 50 Scan spectrophotometer. Absorption spectra were recorded in the range 200 – 1100

195 nm. All measurements were carried out in absorption mode, using the single beam scanning  
196 technique, at a scan rate of 60 nm/min. The thickness of glass samples was  $\sim 2$  mm for all  
197 samples. First-derivative, continuous-wave, and monolithic-specimen EPR spectra were  
198 collected for all glass samples. All EPR measurements were performed using a Bruker EMX  
199 nano EPR spectrometer, at room temperature, at an X-band frequency of  $\sim 9.6$  GHz. The  
200 magnetic field modulation employed was 100 kHz. The microwave power used for the  
201 experiment was 0.3162 mW, with a modulation amplitude of 0.4 mT. The second-order  
202 derivative of the EPR signal was obtained by numerically differentiating the measured first-  
203 order derivative of EPR spectra, which has been used to clarify the  $g$ -values and linewidths  
204 associated with radiation-induced defect-centres.

205  $^{121}\text{Sb}$  Mössbauer spectra were obtained at room temperature (293 K) in transmission  
206 geometry using the 37.2 keV  $\gamma$ -rays from a 0.84 mCi  $\text{CaSn}(^{119}\text{Sb})\text{O}_3$  source mounted on a  
207 constant acceleration drive (SEECO, Edina, MN.). The gamma-rays were detected with a  
208 xenon-filled proportional counter. The velocity scale was calibrated using an  $\alpha$ -Fe absorber  
209 and a  $\text{Rh}^{57}\text{Co}$  source. The absolute source velocity must be slightly adjusted because the  
210  $\text{Rh}^{57}\text{Co}$  source has an isomer shift relative to  $\alpha$ -Fe which requires subtraction of  $0.1 \text{ mm s}^{-1}$ .  
211 The resulting spectra showed two broad lines, one due to  $\text{Sb}^{3+}$  and one due to  $\text{Sb}^{5+}$ , the latter  
212 having a higher absolute velocity. The asymmetry in the  $\text{Sb}^{3+}$  component is due to the  
213 quadrupole splitting of the eight lines in the  $7/2+$  to  $5/2+$  transition in  $^{121}\text{Sb}$ . The  $5+$  line has  
214 no quadrupole splitting since it is spherically symmetrical, so the extra width compared with  
215 the lifetime width of about  $2 \text{ mm s}^{-1}$  reflects the broadening by the different environments in  
216 the glass. We take the  $5+$  to have the same natural width. The spectra were least-square fitted  
217 to extract the hyperfine parameters centre shift ( $\delta$ ), quadrupole interaction ( $e^2\text{Qq}$ ), Lorentzian  
218 linewidth ( $\Gamma$ ), and intensities ( $I$ ) and are shown in Figure 7. The velocity scale shown in  
219 Figure 7 is the as measured velocity. In the literature it is common to quote the centre shift

220 values relative to InSb by adding  $8.6 \text{ mm s}^{-1}$ . Hence the conversion here was  $-0.1+8.6 = +8.5$   
 221  $\text{mm s}^{-1}$  and the corrected values of the centre shift ( $\delta$ ) are given in Table 3, together with the  
 222 other fitted Mössbauer parameters.

### 223 3. Results

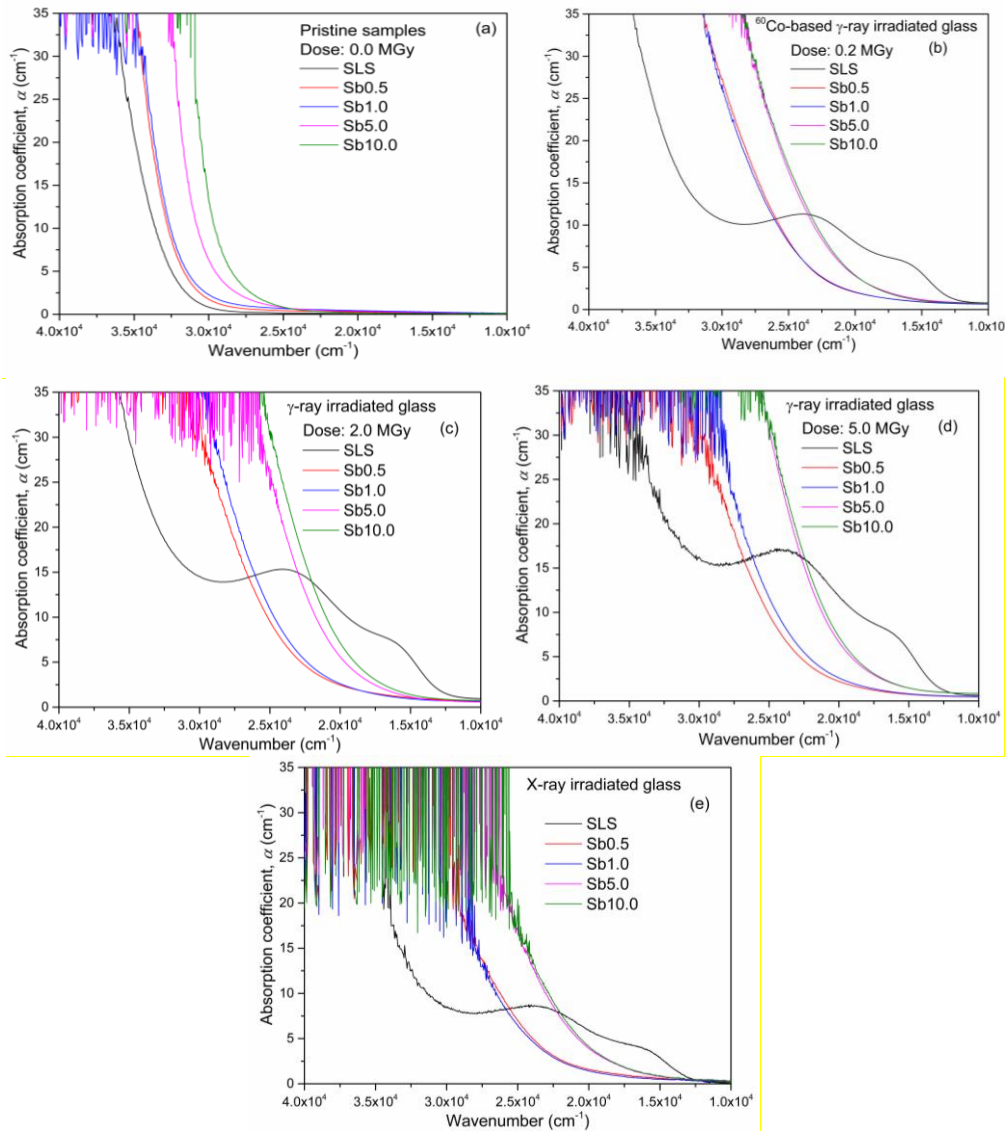


**Figure 1:** Absorption coefficient spectra of (a) pristine (i.e., 0.0 MGy), (b) 0.2 MGy, (c) 2.0 MGy, and (d) 5.0 MGy dose of  $\gamma$ -ray, and (e) X-ray irradiated glass samples.

224 The interactions of high energy ionizing radiation (e.g.,  $\gamma$ -ray, X-ray) with matter resulted in  
 225 generation of free electrons and holes in the network [1,7]. These free electrons and holes  
 226 were trapped either at vacancies, interstitial atoms, and non-bridging oxygens, or captured by  
 227

228 multivalent ions in the network [5]. The incorporation of holes and electrons in the network  
229 leads to *defect centres* in the glass, which preferentially absorb the UV and visible radiation  
230 [1,10,11,19,20,23,29]. *Defect centres* have commonly been labelled *colour centres* by some  
231 authors [1,4,10,11,19,20,23,29]. In several prior studies, UV-visible-nIR optical absorption  
232 spectroscopy and electron paramagnetic resonance (EPR) have been used to analyse  
233 radiation-induced defect centres in glass networks [1,3,11,12,16,18–20,23]. The characteristic  
234 energies and linewidths of radiation-induced optical absorption bands, together with the line  
235 shapes and “g” values from EPR spectra, have been utilized to decipher the origins of specific  
236 defect centres [1,11,12,18–20,23].

237 The absorption spectra of glass samples are influenced by their thickness, governed by  
238 Beer’s law. The influence of sample thickness on the absorption spectra was excluded by  
239 calculating the absorption coefficient for each sample. The absorption coefficient ( $\alpha$ ) was  
240 evaluated using (1):

$$241 \quad \alpha(\varepsilon) = \frac{2.303 \times A(\varepsilon)}{t} \quad (1)$$

242 where  $A(\varepsilon)$  and  $t$  represent the measured absorbance as a function of wavenumber (i.e.,  $\varepsilon$ ) and  
243 thickness of each sample in cm, respectively. The absorbance is measured directly using the  
244 absorption spectrophotometer device. The origin of the constant multiplication factor of  
245 2.303 is described in the Supplementary Information. The induced absorption coefficient for  
246 each irradiated glass was evaluated by subtracting the absorption coefficient of pristine glass  
247 ( $\alpha_p$ ) from the absorption coefficient of its counterpart irradiated glass ( $\alpha_i$ ). Therefore, the  
248 induced absorption coefficient ( $\Delta\alpha$ ) was calculated according to (2):

$$249 \quad \Delta\alpha(\varepsilon) = \alpha_i(\varepsilon) - \alpha_p(\varepsilon) \quad (2)$$

250 The radiation-induced absorption spectra for multicomponent glasses show the  
 251 superposition of several absorption bands from *defect centres*. To assess the contribution of  
 252 each *defect centre* to the induced absorption, the spectra were resolved into multiple Gaussian

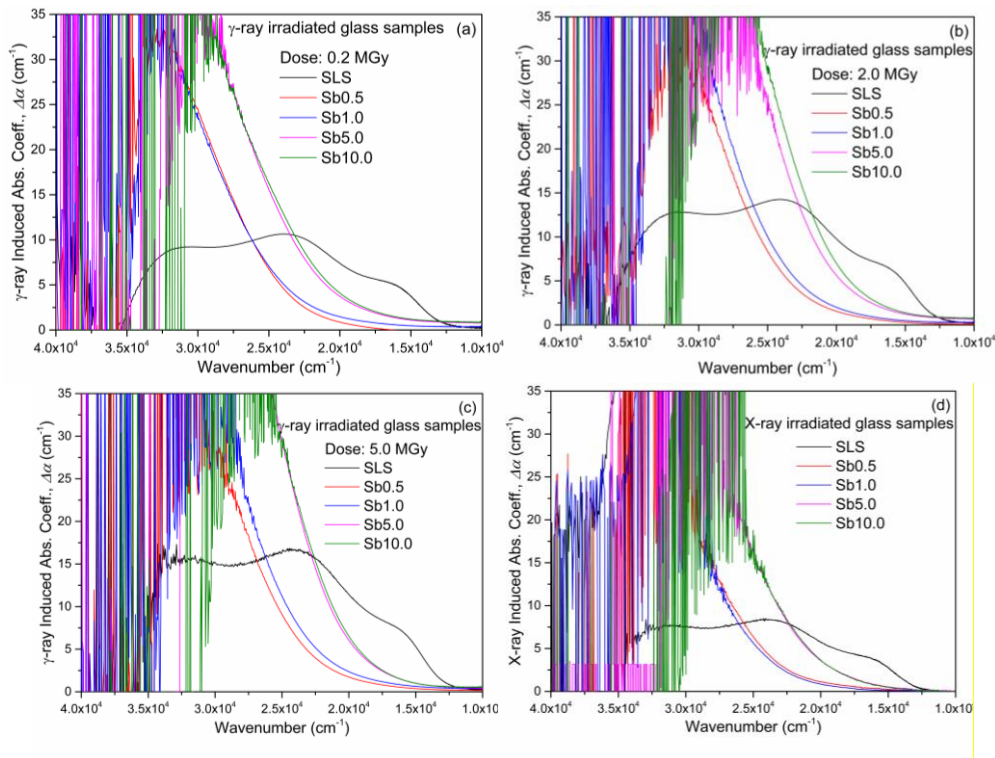


**Figure 2:** Radiation induced absorption coefficient ( $\Delta\alpha$ ) spectra of (a) 0.2 MGy, (b) 2.0 MGy, and (c) 5.0 MGy dose of  $\gamma$ -ray, and (d) X-ray irradiation.

253 bands using OriginPro 9.1 software [1,21,23]. The deconvoluted induced absorption spectra  
 254 reveal the characteristic energy and bandwidth of specific *defect centres* [21,23]. According  
 255 to various reports the deconvolution of radiation-induced absorption coefficients of soda-  
 256 lime-silica glass was resolved into four Gaussian bands [1,23].

257 First-derivative, continuous-wave monolithic sample EPR spectra at room temperature  
 258 were recorded, probing an X-band frequency of  $\sim 9.6$  GHz. The second derivative of the EPR  
 259 signal was calculated to obtain the peak of the EPR absorption signal that was utilized to  
 260 evaluate the  $g$  value of the respective *defect centres*.

261 Employing the optical absorption spectra, the absorption coefficients (i.e.,  $\alpha$ ) of the  
 262 present series of glass samples were assessed using (1). The absorption coefficient spectra of

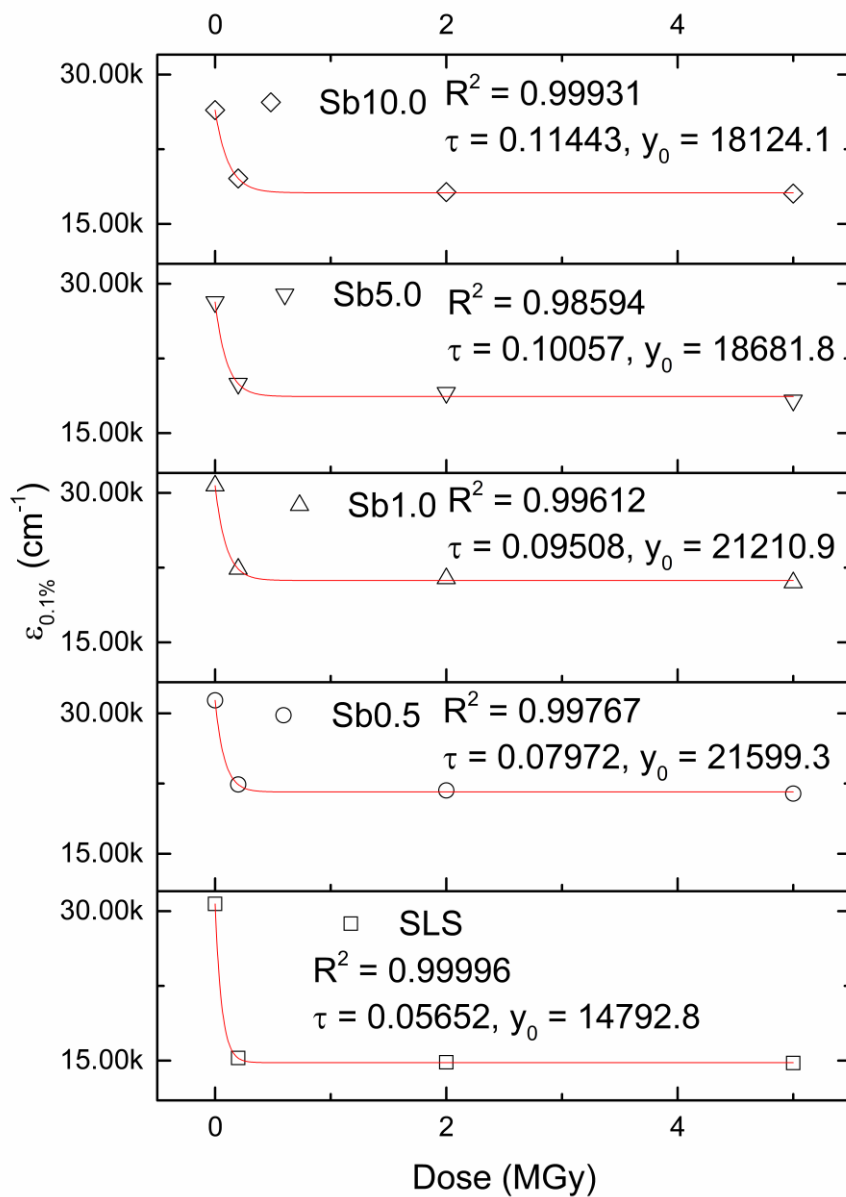


**Figure 3:** Plot of 0.1% transmittance wavenumber (i.e.,  $\epsilon_{0.1\%}$ ) as a function of the  $\gamma$ -ray doses of studied glass samples, fitted with  $y = A \exp(-x/\tau) + y_0$  function.

264 the glass samples before and after various doses of ionizing radiation are illustrated in Figure  
 265 1 (a – e). The absorption coefficient spectra of pristine (0.0 MGy) glass samples are shown in  
 266 Figure 1(a), which reveals the steady redshift of the UV band-edge wavelength with the

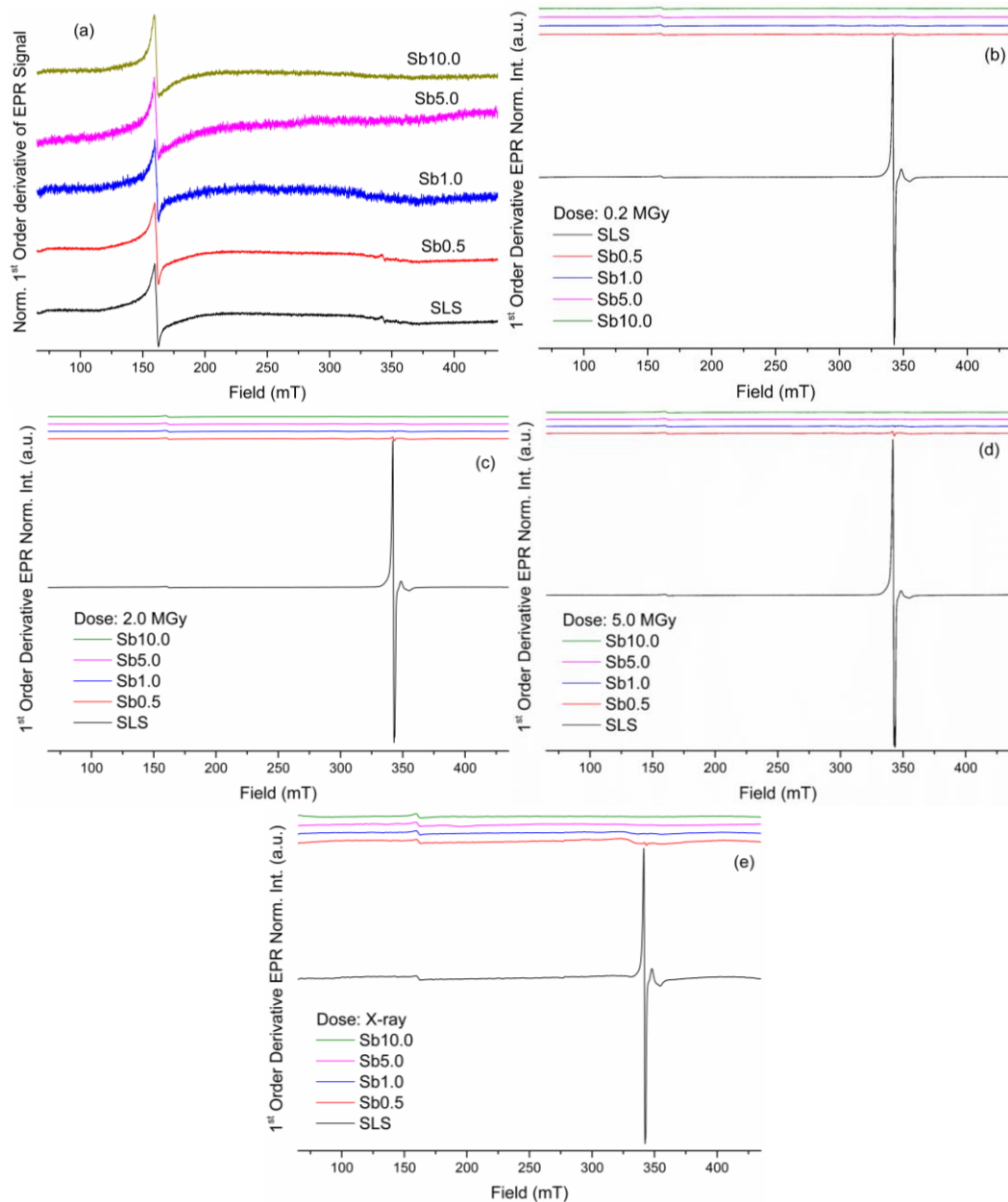


**Figure 4:** Background compensated and normalized first-order derivative of X-band EPR response of (a) pristine, (b) 0.2 MGy, (c) 2.0 MGy, (d) 5.0 MGy dose of  $\gamma$ -ray, and (e) X-ray irradiated glass samples at 298 K.

267 addition of  $\text{Sb}_2\text{O}_3$  to the glass. The exposure of the glass to  $\gamma$ -rays then resulted in a

268 significant modification of the shape function of the absorption coefficient spectra, which are  
269 shown in Figures 1 (b – d). The effects of X-ray exposure to the glass samples are presented  
270 in Figure 1 (e). The glasses manifested the formation of radiation-induced absorption bands  
271 of defect-centres at visible wavelengths following both  $\gamma$ -ray and X-ray exposure. Increasing  
272 dose of  $\gamma$ -rays increased the absorption coefficient of the radiation-induced defect centres.  
273 Notably, the radiation-induced visible optical absorption bands disappeared when  $\text{Sb}_2\text{O}_3$  was  
274 introduced into the glass at all levels of  $\text{Sb}_2\text{O}_3$  addition studied here. To offer a quantitative  
275 analysis of the radiation-induced effects in glass samples, the radiation-induced absorption  
276 coefficient (i.e.,  $\Delta\alpha$ ) spectra were assessed using (2).

277 Figures 2 (a – d) show the radiation-induced absorption coefficient spectra of the glass  
278 samples for  $\gamma$ -ray doses of 0.2, 2.0, and 5.0 MGy, and for X-ray irradiation, respectively.  
279 Notably, the  $\gamma$ -ray and X-ray irradiated SLS glasses reveal a similar pattern of shape  
280 functions, which supports the superposition of several Gaussian bands. The addition of  $\text{Sb}_2\text{O}_3$   
281 to the glass causes a significant modification of the shape function of the absorption  
282 coefficient spectra. The Sb0.5 sample developed a broad and intense absorption band  
283 associated with defect-centres, which possibly has a peak at a deep UV wavelength.  
284 However, the UV band-edge of Sb0.5 glass masked the peak of the respective absorption  
285 band. Further addition of  $\text{Sb}_2\text{O}_3$  to the glass did not alter the shape function of the induced-  
286 absorption spectra. However, increasing of the dose of  $\gamma$ -rays enhanced the width of the  
287 radiation-induced optical absorption band, suggesting an increase in intensity.

288 Figure 3 reveals the effects of irradiation dose of  $\gamma$ -rays on the transmittance of the  
289 glass samples. The wavenumber at which the transmittance of the glass sample (path length  
290 of 1 cm) becomes 0.1% is measured and designated as  $\varepsilon_{0.1\%}$ . The factor  $\varepsilon_{0.1\%}$  is plotted as a  
291 function of the  $\gamma$ -ray dose, which closely follows a first-order exponential decay function, as

292 evidenced by the very high fit  $R^2$  values (Figure 3). Figure 3 also confirms the retention of  
 293 the transmittance of the glass samples after being subjected to ionizing radiation.

294 The absorption coefficient spectra of the series of pristine glasses confirm the  
 295 continuous red shift of the UV cut-off wavelength with increasing additions of  $Sb_2O_3$  to the

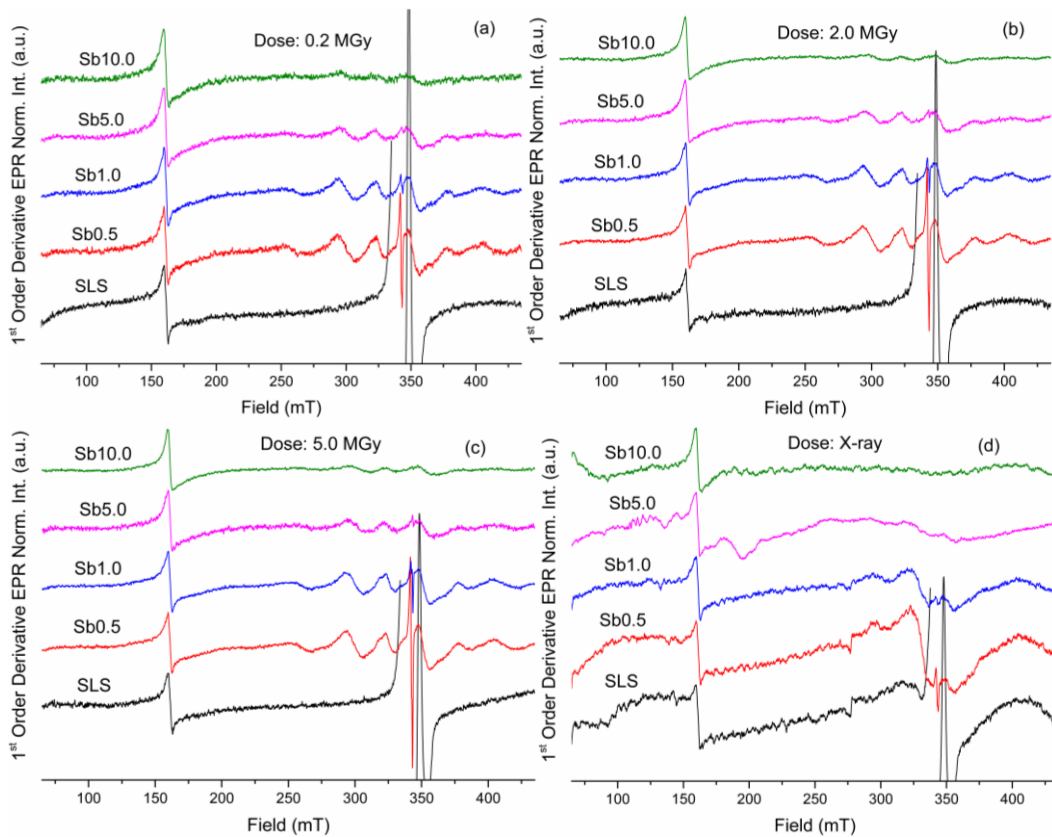


**Figure 5:** The magnified EPR response of glass samples irradiated with (a) 0.2 MGy,  
 (b) 2.0 MGy, (c) 5.0 MGy dose of  $\gamma$ -ray, and (d) X-ray.

296 glass. Supplementary information S – I (a – e) shows the evaluation of UV band-gap energy  
 297 of the present series of glass, for various doses of ionizing radiation using a Tauc plot [77].  
 298 For the evaluation of band-gap energy,  $(ah\nu)^{1/2}$  vs.  $h\nu$  was plotted. Supplementary  
 299 information S – II shows the cut-off energy as a function of nominal  $Sb_2O_3$  content of the  
 300 glass, for pristine, X-ray, and  $\gamma$ -ray irradiated glasses. In general, increasing dose of ionizing  
 301 radiation steadily reduces the cut-off energy, in comparison to the pristine samples.

302            Figures 4 (a – e) reveal the background-compensated and normalized first-order  
303 derivatives of the X-band EPR spectra at ambient temperature ( $\sim 298$  K) for the series of  
304 glass samples, for various doses of ionizing radiation. The EPR spectra reveal the hyperfine  
305 signals in (i) the 140 – 170 mT range; and (ii) the 250 – 435 mT range. For the 140 – 170 mT  
306 range, a signal was reported around 160 mT ( $g \sim 4.28$ ) for every sample, which is consistent  
307 with rhombically-distorted isolated sites  $\text{Fe}^{3+}$ -ion impurities [78,79]. For the present study,  
308  $\text{Fe}^{3+}$ -ions were probably introduced as impurities in the glass making raw materials, and  
309 particularly the silica sand used in this study, at ppm levels. As a result, the

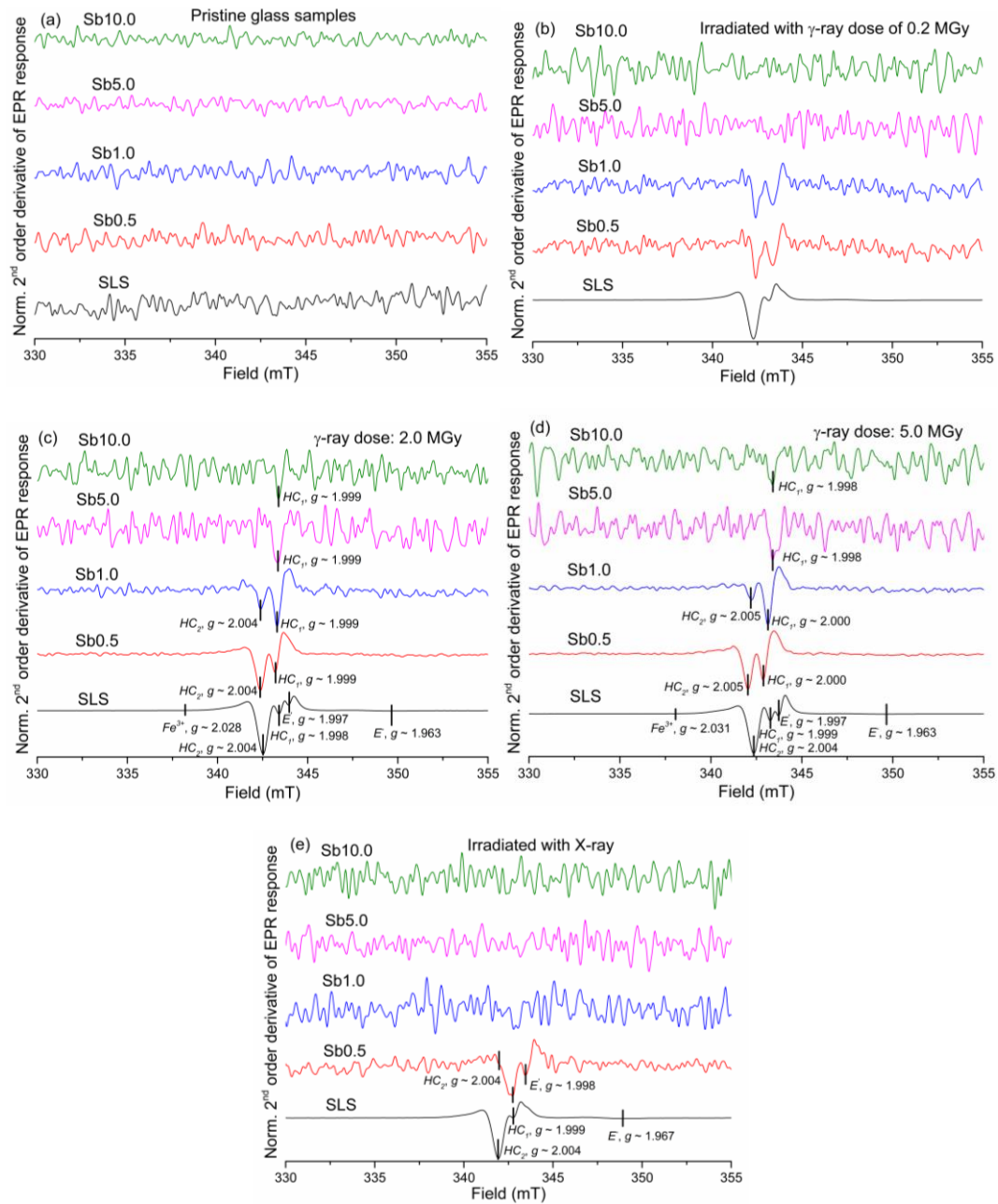


**Figure 6:** Normalized second-order derivative of EPR spectra of (a) pristine, (b) 0.2 MGy, (c) 2.0 MGy, (d) 5.0 MGy dose of  $\gamma$ -ray, and (e) X-ray irradiated glass samples.

310

311 normalization of the first-order derivative EPR spectra was performed for the peak-to-peak  
312 intensity of  $\text{Fe}^{3+}$  signal (160 mT;  $g \sim 4.28$ ). Figure 4 (a) reveals the EPR spectra of pristine

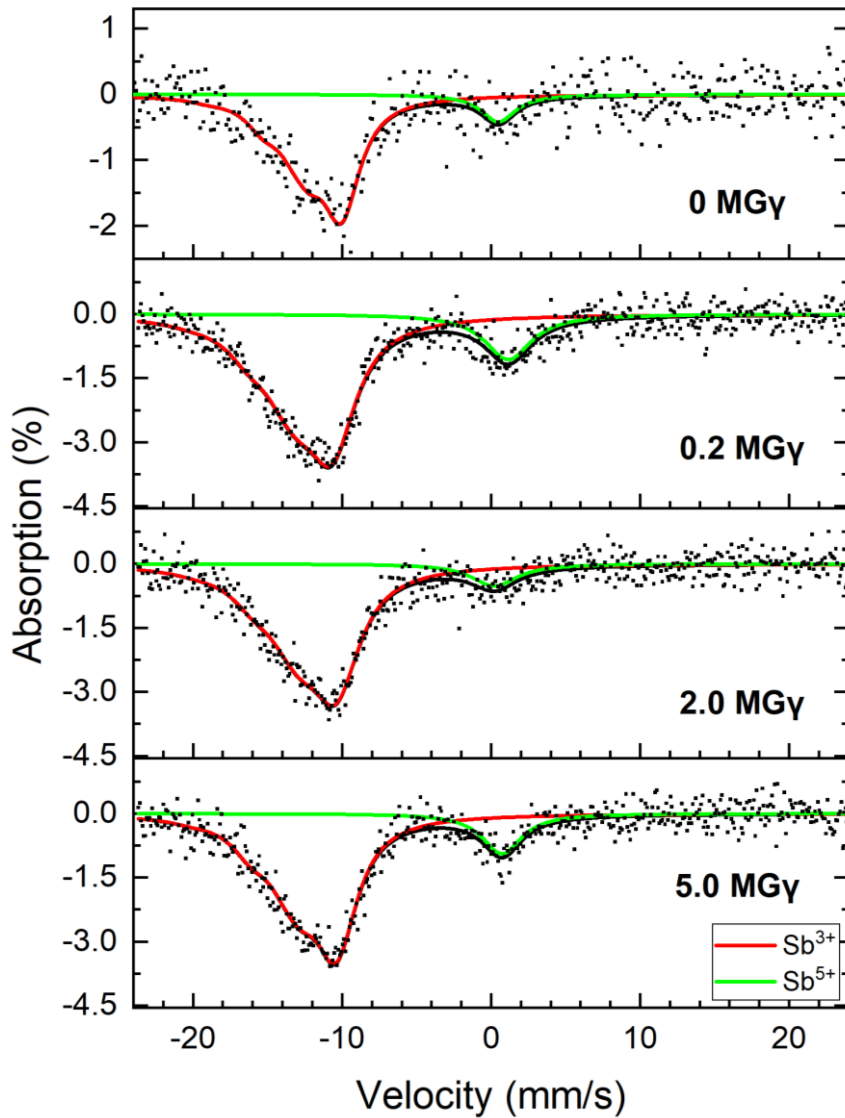


**Figure 7:**  $^{121}\text{Sb}$  Mössbauer spectra (293 K) for sample Sb10.0, irradiated with 0.2, 2.0, and 5.0 MGy of  $\gamma$ -rays.

313 glass samples. Notably, for the pristine samples a very weak, asymmetric and broad EPR  
314 trace in the range 300 – 420 mT ( $g \sim 2.0$ ) was detected (Figure 4(a)), which is attributed to  
315  $\text{Fe}^{3+}$ - $\text{Fe}^{3+}$  interactions in the glass network [79]. Given the ppm levels of Fe in the glass, such  
316 interactions are very weak. Nevertheless, there may be a slight decrease in the intensity of the  
317  $g \sim 2.0$  signal with increasing  $\text{Sb}_2\text{O}_3$  content. Figures 4 (b – d) reveal the EPR spectra of glass  
318 samples subjected to 0.2, 2.0, and 5.0 MGy doses of  $\gamma$ -ray, respectively. Figure 4 (e) reveals

319 the EPR spectra of glass samples, which were exposed to X-rays. Figures 4 (b – e) have thus  
 320 confirmed the formation of ionizing radiation-induced defect-centres in the glass network.  
 321 The  $\gamma$ -ray or X-ray induced spectra reveal a set of intense, sharp, and overlapping EPR

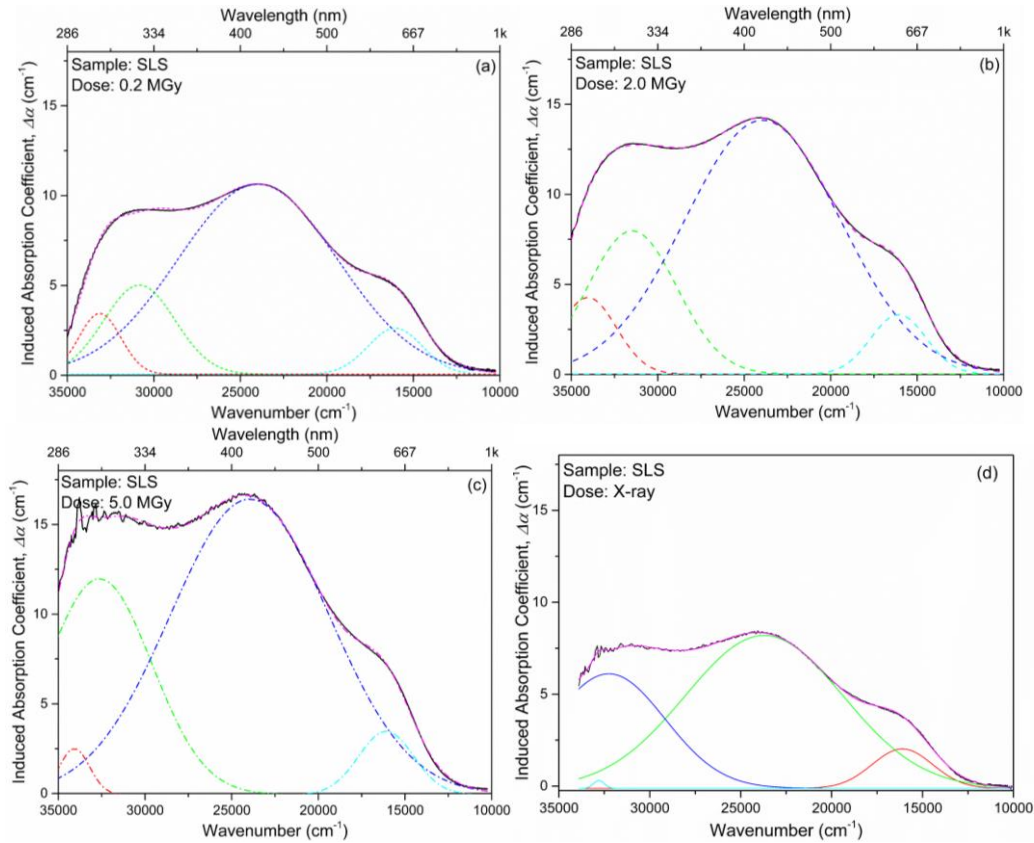


**Figure 8:** The deconvolution of radiation-induced absorption coefficient of SLS base glass for (a) 0.2 MGy, (b) 2.0 MGy, and (c) 5.0 MGy dose of  $\gamma$ -rays and (d) X-rays.

322 signals in the range 330 – 355 mT (Figures 4, 5 and 6). However, the systematic addition of  
 323  $\text{Sb}_2\text{O}_3$  to the glass significantly reduces the intensity of these EPR responses from irradiated  
 324 glasses in the 330 – 355 mT range. To aid our study of the effects of ionizing radiation for  
 325  $\text{Sb}_2\text{O}_3$ -modified SLS glass samples, the series of EPR spectra were magnified and shown in  
 326 Figures 5 (a – d).

327 **Table 1: The parameters associated with deconvolution of radiation-induced defect centres of SLS glass:**  
 328 **Goodness of fit ( $R^2$ ), characteristic peak energy ( $E$ ), FWHM ( $\Delta E$ ), and area under the absorption band**  
 329 **( $A$ ) with the partial fraction of area under the band are in the parenthesis.**

Defect Type	Dose →	0.2 MGy	2.0 MGy	5.0 MGy	X-ray
	$R^2$	0.99948	0.99971	0.99959	0.99966
$HC_2$ + $POR$	$E_1$ (cm <sup>-1</sup> )	16050	16050	16050	16130
	$\Delta E_1$ (cm <sup>-1</sup> )	3710	3790	3710	3870
	$A_1$ (eV×cm <sup>-1</sup> )	1.26 (6.1%)	1.64 (5.5%)	1.74 (4.7%)	1.11 (6.0%)
$HC_1$	$E_2$ (cm <sup>-1</sup> )	24030	23950	23950	23710
	$\Delta E_2$ (cm <sup>-1</sup> )	10810	10650	10810	10160
	$A_2$ (eV×cm <sup>-1</sup> )	15.1 (72.6%)	19.7 (65.7%)	23.5 (63.1%)	11.2 (61.1%)
$TE$	$E_3$ (cm <sup>-1</sup> )	30810	31450	32660	32260
	$\Delta E_3$ (cm <sup>-1</sup> )	4840	6130	7100	7260
	$A_3$ (eV×cm <sup>-1</sup> )	3.18 (15.2%)	6.40 (21.3%)	11.31 (30.4%)	5.98 (32.6%)
$Unknown$	$E_4$ (cm <sup>-1</sup> )	33150	34040	34040	32830
	$\Delta E_4$ (cm <sup>-1</sup> )	2900	3870	2100	730
	$A_4$ (eV×cm <sup>-1</sup> )	1.28 (6.1%)	2.19 (7.3%)	0.70 (1.9%)	0.04 (0.2%)

330 Notably, the spectra for the  $\gamma$ -ray irradiated glasses confirm the presence of a second  
331 type of EPR resonance, which has a very broad and diffuse EPR response across the range  
332 250 – 435 mT, as shown in Figures 5 (a – c). The occurrence of these broad EPR responses  
333 was verified from the integrated EPR absorption spectra of the series of  $\gamma$ -ray irradiated glass  
334 samples, which have been shown in the supplementary information S – III (a – c). The peaks  
335 of these broad EPR absorption bands of  $\gamma$ -ray induced  $\text{Sb}_2\text{O}_3$ -modified SLS glass were  
336 observed at 260.6 mT ( $g \sim 2.63$ ), 301.8 mT ( $g \sim 2.27$ ), 326.6 mT ( $g \sim 2.10$ ), 351.6 mT ( $g \sim$   
337 1.95), 381.3 mT ( $g \sim 1.80$ ), and 411.0 mT ( $g \sim 1.67$ ), respectively. The peak position, shape  
338 function, and relative intensity ratio of various hyperfine transitions of EPR absorption  
339 spectra are consistent with the EPR spectrum of  $\text{Sb}^{4+}$  ions in a silicate glass host, as reported  
340 by Schreurs and Davis [80]. The strongest relative EPR absorption intensity from these  $\text{Sb}^{4+}$   
341 ions was observed for the Sb0.5 sample, and it weakens progressively with further addition of

342  $\text{Sb}_2\text{O}_3$  to the glass. Figure 5 (d) also confirms the non-existence of  $\text{Sb}^{4+}$  ions in the X-ray  
 343 irradiated  $\text{Sb}_2\text{O}_3$ -modified SLS glass.

344 To analyse the sharp and intense EPR response in the range 330 – 355 mT, the second-  
 345 order derivatives of the EPR spectra were evaluated and shown in Figure 6 (a – e). The ‘ $g$ -  
 346 values’ of the defect sites were found from the local minima of the second-order derivatives  
 347 of EPR spectra. The ionizing radiation-induced SLS glass spectra reveal sharp and intense

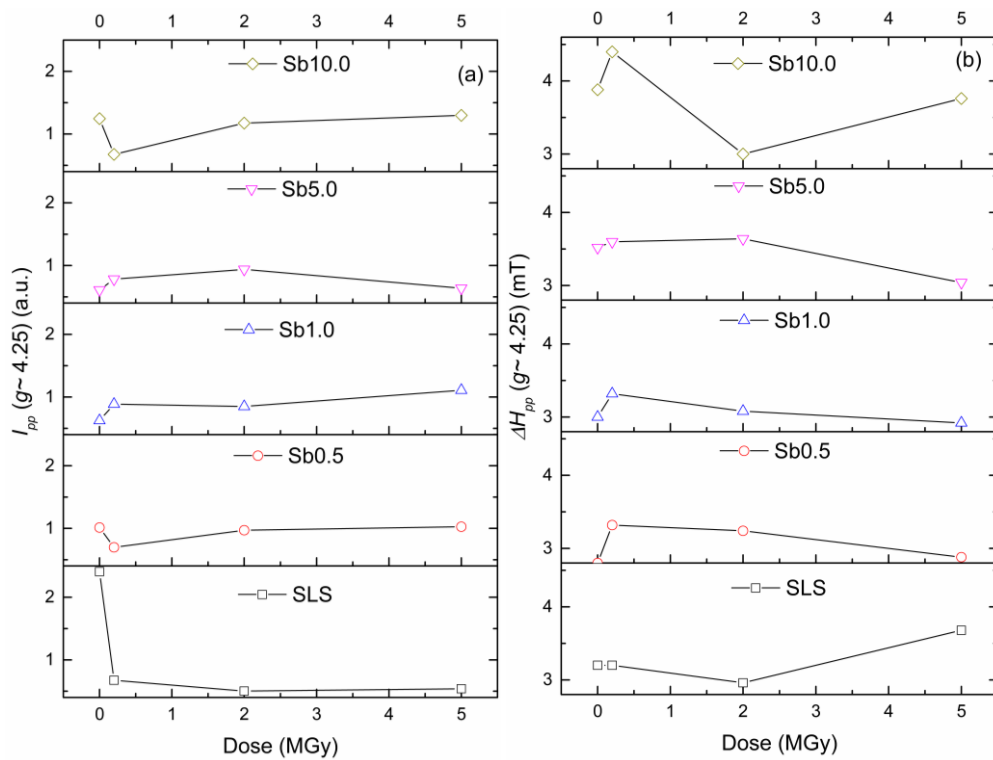


**Figure 9:** EPR hyperfine signal (a) peak-to-peak intensity ( $I_{pp}$ ) and (b) peak-to-peak line width ( $\Delta H_{pp}$ ) of ( $g \sim 4.25$ ) signal at various doses of  $\gamma$ -ray irradiation.

348 bands in the EPR spectra, within the 330 – 355 mT range of the magnetic field. The addition  
 349 of  $\text{Sb}_2\text{O}_3$  to the glass significantly reduces the intensity of the EPR response in the 330 – 355  
 350 mT range.

351 Figure 7 shows the fitted  $^{121}\text{Sb}$  Mössbauer spectra for sample Sb10.0, irradiated with  
 352 0.2, 2.0, and 5.0 MGy of  $\gamma$ -rays. The spectra have two major components, which exhibit the  
 353 characteristics of  $\text{Sb}^{3+}$  (a broad asymmetric component) and  $\text{Sb}^{5+}$  (narrow symmetric  
 354 component) ions [74]. No component representing  $\text{Sb}^{4+}$  could be reliably fitted, given its low

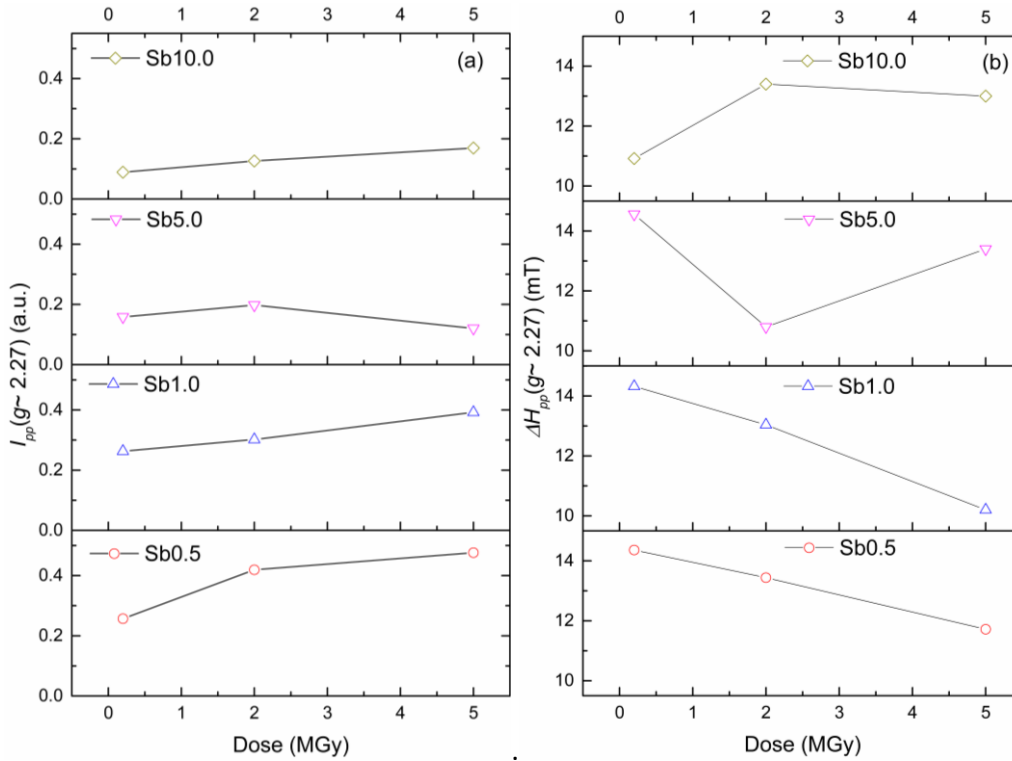


**Figure 10:** The hyperfine (a) peak-to-peak intensity ( $I_{pp}$ ), (b) peak-to-peak linewidth ( $\Delta H_{pp}$ ) of  $g \sim 2.27$  signal.

355 abundance, as indicated by EPR spectra.

356 **Table 2: EPR analysis of defects induced by  $\gamma$ -ray irradiation, signal peak position in mT, respective  $g$ -**  
 357 **factor and width of the respective signal in mT.**

Sample	Defect type	0.2 MGy			2.0 MGy			5.0 MGy		
		Peak (mT)	$g$	W (mT)	Peak (mT)	$g$	W (mT)	Peak (mT)	$g$	W (mT)
SLS	$HC_2$	342.28	2.0050	1.87	342.36	2.0036	1.80	342.36	2.0045	1.94
	$HC_1$	343.12	2.0001	0.28	343.28	1.9985	0.42	343.28	1.9992	0.70
	$E'$				343.72	1.9966	0.70	343.72	1.9966	0.70
	$E$	349.44	1.9639	4.15	349.44	1.9628	3.88	349.44	1.9639	3.88
Sb0.5	$HC_2$	342.40	2.0043	1.25	342.24	2.0043	1.25	342.24	2.0052	1.39
	$HC_1$	343.36	1.9987	1.52	343.12	1.9989	1.52	343.12	2.0001	1.52

Sb1.0	$HC_2$	342.40	2.0043	1.25	342.24	2.0045	1.38	342.24	2.0052	1.38
	$HC_1$	343.36	1.9987	1.52	343.12	1.9989	1.66	343.12	2.0001	1.66
Sb5.0	$HC_1$	-	-	-	343.36	1.9985		343.40	1.9987	
Sb10	$HC_1$	-	-	-	343.36	1.9985		343.40	1.9987	

358

359 Figure 8 (a – d) shows the radiation-induced optical absorption spectra, which reveal  
360 the superposition of absorption bands related to different defect centres. Spectra were  
361 deconvoluted into 4 Gaussian bands, which was the minimum needed for robust fitting.  
362 Fitting parameters such as characteristic energy ( $E_i$ ), bandwidth ( $\Delta E_i$ ), with the area ( $A_i$ ) and a  
363 respective partial fraction of the area under the absorption spectrum, are presented in Table 1.  
364 A partial fraction of the area under a certain Gaussian curve associated with a specific defect-  
365 centre is roughly representing the quantitative formation of a certain defect type, although full  
366 quantification is not possible without knowledge of the extinction coefficients associated with  
367 each individual defect type. This reveals the characteristic peak energies at about 16,000  $\text{cm}^{-1}$   
368 ( $\sim 620$  nm) and 24,000  $\text{cm}^{-1}$  ( $\sim 420$  nm), which remained almost unaltered for different doses  
369 of  $\gamma$ -rays and X-rays. The subsequent band has a characteristic wavenumber of about 30,800  
370  $\text{cm}^{-1}$  (325 nm) for a 0.2 MGy dose. The peak characteristic energy shifted slightly to 31,400  
371  $\text{cm}^{-1}$  (318 nm) and 32,600  $\text{cm}^{-1}$  (307 nm) for 2.0 and 5.0 MGy doses, respectively. The other  
372 Gaussian band had a characteristic energy of 33,000–34,000  $\text{cm}^{-1}$ . Based on prior studies,  
373 the induced absorption band at  $\sim 16,000$   $\text{cm}^{-1}$  appears to be associated with non-bridging-  
374 oxygen hole centres ( $NBOHC$  or  $HC_2$ ) along with peroxy-radicals ( $POR$ ) [1,9,10,23,58]. The  
375 structure of  $HC_2$ -type defect centres could be explained as a dangling oxygen atom with an  
376 unpaired electron, (i.e.,  $HC_2 \rightarrow \equiv\text{Si}-\dot{\text{O}}$ , where ‘ $\equiv$ ’ represents three bonds with other oxygens  
377 in the network and ‘ $\cdot$ ’ depicted as the unpaired electron) [10,14,20].

378 **Table 3: Refined  $^{121}\text{Sb}$  Mössbauer parameters (293 K) of the Sb10.0 sample irradiated**  
379 **with a various dose of  $\gamma$ -ray: centre shift relative to InSb ( $\delta$ ), Lorentzian line width ( $\Gamma$ ),**  
380 **quadrupole interaction ( $e^2Qq$ ), Intensity ( $I$ ).**

$\gamma$ -ray dose		0.0 MGy	0.2 MGy	2.0 MGy	5.0 MGy
Sb <sup>3+</sup>	$\delta_1$ (mm s <sup>-1</sup> )	-3.2	-3.8	-3.4	-3.5
	$\Gamma_1$ (mm s <sup>-1</sup> )	3.54	3.80	3.74	3.24
	e <sup>2</sup> Qq (mm s <sup>-1</sup> )	18.9	18.8	19.9	20.5
	$I_1$ (%)	88	83	90	85
Sb <sup>5+</sup>	$\delta_2$ (mm s <sup>-1</sup> )	9.1	9.4	8.6	9.2
	$\Gamma_2$ (mm s <sup>-1</sup> )	3.56	3.82	3.74	3.22
	$I_2$ (%)	12	17	10	15

381

382 According to Zatsepin *et al.* [20], the optical absorption band centred at  $\sim 16,000$  cm<sup>-1</sup>  
383 for the  $HC_2$  formed because of the transition of an electron from the  $\sigma$ -orbital to a half-filled  
384  $p$ -orbital between the atoms of nonbridging oxygen and silicon [20]. The peak at  $\sim 24,000$   
385 cm<sup>-1</sup> confirms the occurrence of an  $HC_I$ -type defect centre [3,10,21,23]. The  $HC_I$ -type defect  
386 centre is created because of the dangling bond of  $\equiv\text{Si}-\dot{\text{O}}$  and Na<sup>+</sup> ions (i.e.  $HC_I \rightarrow \equiv\text{Si}-$   
387  $\dot{\text{O}}\dots\text{Na}^+$ , where ‘...’ presents the dangling bond) [14,20]. The defects induced by the self-  
388 trapped electrons (i.e.,  $STE \rightarrow \equiv\text{Si}-\dot{\text{O}}-\text{Si}\equiv$ ) have been attributed to the absorption band at  
389  $30,800 - 32,600$  cm<sup>-1</sup> [10,21,23]. Unlike the  $NBOHC$  and  $HC_I$  defect centres, the  $STE$ -type  
390 defect involves bridging oxygens (i.e.,  $BO$ ), each with an unpaired electron. However, the  
391 origin of the band fitted at  $33,000 - 34,000$  cm<sup>-1</sup> is less clear. Polaron  $E^-$ -type negative  
392 electron centres originate from the capture of an electron by a silicon atom (i.e.,  $E^- \rightarrow \equiv\text{Si}\cdot$ ),  
393 which has a UV absorption band of characteristic wavenumber of  $41,000 - 44,000$  cm<sup>-1</sup>  
394 [1,10]. However, in the present study, the UV band-edge of the host (i.e., SLS) glass was  
395 found at about  $35,000$  cm<sup>-1</sup>, which masked any deep UV-absorption bands that may have  
396 been attributable to  $E^-$ -polarons. The absolute area under defect-induced absorption bands  
397 increased steadily with radiation dose. However, the relative partial area of  $HC_2$  and  $HC_I$ -  
398 type defect centres was reduced due to the increased formation of  $STE$ -type defect centres

399 with increasing  $\gamma$ -ray dose. This implies that increased  $\gamma$ -ray dose resulted in more *STE*-type  
400 defects, relative to the *HC<sub>2</sub>* and *HC<sub>1</sub>* defect types.

401 Figures 9 (a) and (b) reveal the effects of  $\gamma$ -ray exposure on the  $g \sim 4.28$  EPR signal,  
402 associated with  $\text{Fe}^{3+}$  impurity ions, for the present series of glasses. Figure 9 (a) reveals the  
403 peak-to-peak intensity of  $\text{Fe}^{3+}$  ions using  $g \sim 4.28$  signal (i.e.,  $I_{pp}$ ) as a function of  $\gamma$ -ray dose.  
404 The peak-to-peak linewidth of the  $g \sim 4.28$  signal of  $\text{Fe}^{3+}$  ions (i.e.,  $\Delta H_{pp}$ ) at various  $\gamma$ -ray  
405 doses, is shown in Figure 9 (b).

406 Figures 10 (a) and (b) show the effects of  $\gamma$ -ray dose on the EPR signal from  $\text{Sb}^{4+}$  ions.  
407 Figure 10 (a) portrays the hyperfine signal peak-to-peak intensity ( $I_{pp}$ ) of the  $g \sim 2.27$  signal  
408 at various doses of  $\gamma$ -rays. The Sb0.5 sample spectrum reveals the maximum peak-to-peak  
409 intensity ( $I_{pp}$ ) for the  $g \sim 2.27$  signal, which implies that the relative concentration of  $\text{Sb}^{4+}$   
410 ions may be highest in the Sb0.5 sample. Increasing  $\text{Sb}_2\text{O}_3$  content in the glass steadily  
411 reduced the intensity of the EPR signal linked with  $\text{Sb}^{4+}$  ions at various doses of  $\gamma$ -rays (see  
412 also Figure 5).

413

#### 414 **4. Discussion**

415 One factor affecting the optical band-edge in the pristine glasses is the broad spin-  
416 forbidden absorption transition of  $\text{Sb}^{3+}$ :  $^1S_0 \rightarrow ^3P_1$  centred at  $40,000 - 46,000 \text{ cm}^{-1}$  [5, 7, 74].  
417 Increasing additions of  $\text{Sb}_2\text{O}_3$  to the glass network have continuously red-shifted the UV  
418 band-edge, as explained and discussed in our previous paper [74]. The absorption of  
419 increasing doses of  $\gamma$ -radiation causes narrowing of the forbidden band gap. Baccaro *et al.* [9]  
420 also observed the forbidden band gap narrowing with increasing dose of  $\gamma$ -radiation in  
421 multicomponent borosilicate radiation-hard glass containing cerium [9]. This phenomenon

422 was explained by the accumulation of density of defect states between the valence and  
423 conduction bands of the glass matrix [9].

424 The inclusion of  $\text{Sb}_2\text{O}_3$  in the glass studied here masked the absorption bands of energy  
425 greater than approximately  $27,000 \text{ cm}^{-1}$ , because of the aforementioned significant redshift of  
426 the band-edge. Therefore, the EPR analysis of the present series of glass samples is  
427 paramount. The EPR response of radiation-induced SLS glasses reveals the defect-induced  
428 signals for the 330 – 355 mT range. The second-order derivative of the EPR response was  
429 employed to decipher peak positions and evaluate their width. An EPR peak at around  $g \sim$   
430 2.03 may be associated with clustered  $\text{Fe}^{3+}$  ions, although as noted previously the very low  
431 concentrations (ppm) of Fe in the glass make this EPR resonance extremely weak [78]. The  
432 EPR peak obtained around  $g \sim 2.004$  is attributed to the  $NBOHC$  or  $HC_2$  [20]. The peak  
433 obtained around  $g \sim 1.999$  is assigned to the  $HC_1$ -type of defect-centre [20]. The peak  
434 obtained at  $g = 1.9966$  was identified as an  $E'$ -type defect-centre [20,81]. According to prior  
435 reports, the  $E'$ -type defect has a UV absorption band peak around  $44,500 \text{ cm}^{-1}$ , which lies  
436 within the band-edge of the studied samples [21,23]. The relatively weak signal around  $g \sim$   
437 1.964 is recognized as the  $E^-$ -centre type of defect [20]. The  $E^-$ -centre signifies the polaron,  
438 which consists of a  $\text{Na}^+$  ion with an electron trapped near it [82]. The addition of  $\text{Sb}_2\text{O}_3$  to the  
439 glasses significantly altered the shape functions and intensity of various defect-centres.  
440 Compared to the Sb-free glass, the 0.5 mol% of  $\text{Sb}_2\text{O}_3$  addition significantly diminished the  
441 intensity of both  $HC_1$  and  $HC_2$  defect-centres. The trace of  $E'$  and  $E^-$  defect centres is non-  
442 obvious for the Sb0.5 sample. On the other hand, the EPR study confirmed the occurrence of  
443  $\text{Sb}^{4+}$  ions. Further increase of  $\text{Sb}_2\text{O}_3$ -content of the glass steadily reduced the intensity of  $HC_1$   
444 and  $HC_2$  defect-centres. Unlike  $\text{Sb}^{4+}$ -ions, the  $\text{Sb}^{3+}$  and  $\text{Sb}^{5+}$  ions have no unpaired electrons,  
445 therefore give no EPR signals. However, whilst Mössbauer spectroscopy confirmed they  
446 were both present in substantial quantities, no component for  $\text{Sb}^{4+}$  could be fitted to the

447 Mössbauer spectra, indicating the relative abundance of  $\text{Sb}^{4+}$  cations in all glasses to be very  
448 low (also supported by the intensity of the EPR  $\text{Sb}^{4+}$  component compared with the  $\text{Fe}^{3+}$   
449 signal at  $g \sim 4.28$ , known to be due to ppm levels for  $\text{Fe}^{3+}$  and hence the corresponding  $\text{Sb}^{4+}$   
450 concentrations can also be assumed to be at ppm levels).

451 The peak-to-peak intensity of the  $\text{Fe}^{3+}$  EPR resonance at  $g \sim 4.28$  is proportional to the  
452 concentration of  $\text{Fe}^{3+}$  ion present in the network at such concentrations. Notably, compared to  
453 the pristine glass, 0.2 MGy dose of  $\gamma$ -ray exposure caused a decrease of  $\text{Fe}^{3+}$  intensity for the  
454 present series of samples. This implies that the  $\text{Fe}^{3+}$  ions in the glass network may initially act  
455 as electron trapping centres to follow the  $\text{Fe}^{3+} + e^- \rightarrow \text{Fe}^{2+}$  redox reaction. The growth of  
456  $\text{Fe}^{2+}$ -ions over  $\text{Fe}^{3+}$  could be confirmed from the absorption spectra reported [79,83].  
457 Supplementary information S-IV (a – e) revealed the absorption coefficient spectra extended  
458 up to the infrared region with the Urbach's band tail to obtain the background compensated  
459 absorption coefficient of trace elements (i.e.,  $\text{Fe}^{3+}$  and  $\text{Fe}^{2+}$  ions) [84]. The background  
460 compensated absorption coefficient spectra of  $\text{Fe}^{3+}$  and  $\text{Fe}^{2+}$  ions are depicted in  
461 supplementary information S-V (a – c). Ades *et al.* [85] and Bingham *et al.* [83,84] have  
462 linked various absorption bands of  $\text{Fe}^{3+}$  and  $\text{Fe}^{2+}$  ions for the soda-lime-silica network [85].  
463 The major absorption transitions are designated as: A.  $\text{Fe}^{3+}: {}^6A_1(S) \rightarrow {}^4E_g(D) \sim 26300 \text{ cm}^{-1}$ ,  
464 B.  $\text{Fe}^{3+}: {}^6A_1(S) \rightarrow {}^4A_1(G) \sim 24200 \text{ cm}^{-1}$ , and C.  $\text{Fe}^{2+}: {}^5E_g(D) \rightarrow {}^5A_1(D) \sim 9400 \text{ cm}^{-1}$ . For the  
465 present study, UV absorption bands of  $\text{Fe}^{3+}$  ions (i.e.,  $\text{Fe}^{3+}: {}^6A_1(S) \rightarrow {}^4E_g(D)$  and  $\text{Fe}^{3+}: {}^6A_1(S) \rightarrow {}^4A_1(G)$ )  
466 are identified for the pristine glass samples, which become masked by the  $\gamma$ -  
467 ray induced defect-centres. But the absorption band of  $\text{Fe}^{2+}: {}^5E_g(D) \rightarrow {}^5A_1(D)$  in the infrared  
468 region is identified for the pristine and  $\gamma$ -ray exposed samples. Notably, 0.2 MGy dose of  $\gamma$ -  
469 rays caused significant enhancement of the absorption coefficient of  $\text{Fe}^{2+}: {}^5E_g(D) \rightarrow {}^5A_1(D)$   
470 band for all the glass samples. This is consistent with the decrease of EPR peak-to-peak  
471 intensity of the  $g \sim 4.28$  resonance, which implies a decrease of  $\text{Fe}^{3+}$  ion concentration and

472 increase in  $\text{Fe}^{2+}$  concentration for 0.2 MGy dose. Figure S-V (a) reveals the decrease of the  
 473 absorption coefficient of  $\text{Fe}^{2+}: {}^5T_5(D) \rightarrow {}^5T_3(D)$  band with the enhanced dose (i.e., 2.0 and  
 474 5.0 MGy) of  $\gamma$ -rays, which is consistent with the EPR peak-to-peak intensity of  $g \sim 4.28$   
 475 signal. The absorption bandwidth of  $\text{Fe}^{2+}$  ions has reduced considerably with the  $\gamma$ -ray  
 476 exposure of the glass network. The evolution of the peak-to-peak intensity of  $g \sim 4.28$  signal  
 477 of EPR for Sb0.5 and Sb1.0 sample for various doses of  $\gamma$ -rays has supported the background  
 478 compensated absorption coefficient of  $\text{Fe}^{2+}$  ion. For the Sb5.0 and Sb10.0 samples the  
 479 absorption band tail does not follow Urbach's equation, and the absorption contribution of  
 480  $\text{Fe}^{2+}$  ions are reported in the supplementary information. The peak-to-peak linewidth ( $\Delta H_{pp}$ )  
 481 of the  $g \sim 4.28$  signal results from the separation of three Kramer's doublet transitions  $d_{xx}$ ,  $d_{yy}$ ,  
 482 and  $d_{zz}$ , which are not overlapping with each other [79]. The linewidth of  $g \sim 4.28$  signal for  
 483 SLS glass has reduced for 0.2 MGy dose and increased for 5.0 MGy dose of radiation. For  
 484 Sb0.5 and Sb1.0 samples the linewidth of the  $g \sim 4.28$  signal has not varied considerably at  
 485 various doses of  $\gamma$ -rays. For the Sb5.0 sample, the linewidth of  $g \sim 4.28$  signal remains  
 486 roughly unaltered up to 2.0 MGy of  $\gamma$ -ray, then it reduced at 5.0 MGy dose.

487 In this study, the decay of the  ${}^{60}\text{Co}$  nucleus, employed as the source of  $\gamma$ -rays, offers  $\gamma$ -  
 488 photons of 1.17 and 1.33 MeV [86], with  $\gamma$ -photons with energy more than 1.02 MeV being  
 489 necessary to trigger pair-production [87]. The pair-production process causes the creation of  
 490 an electron ( $e^-$ ) and positron/hole ( $h^+$ ) pair. The  $\text{Sb}^{3+}$ -ions in the SLS network operate as hole  
 491 ( $h^+$ ) trapping centres in the network. The hole in the glass network follows the redox reaction  
 492  $\text{Sb}^{3+} + h^+ \rightarrow \text{Sb}^{4+}$  [60]. As a result, the  ${}^{60}\text{Co}$  nucleus related  $\gamma$ -rays interacting with  $\text{Sb}_2\text{O}_3$ -  
 493 modified SLS glass form the  $\text{Sb}^{4+}$ -ions. At the lowest concentrations of  $\text{Sb}_2\text{O}_3$  in the glass,  
 494 there is large Sb-Sb ion-ion separation, which prevents the majority of  $\text{Sb}^{4+}$  ions from  
 495 interacting with nearby or adjacent  $\text{Sb}^{4+}/\text{Sb}^{3+}$ -ions. As a result, newly-formed  $\text{Sb}^{4+}$  ions  
 496 cannot readily transform to  $\text{Sb}^{3+}$  or  $\text{Sb}^{5+}$  ions. An increased amount of Sb in the SLS glass

497 network reduces the average Sb-Sb ion-ion separation: as demonstrated, for example, by prior  
498 studies of  $\text{Fe}^{3+}$  in SLS type glass, exchange interactions become dominant at concentrations  
499 greater than approximately 1 mol% [88,89,90]. Therefore, we can surmise that as the  $\text{Sb}_2\text{O}_3$   
500 content of the glasses studied here increases, the  $\text{Sb}^{4+}$  ions are increasingly likely to have  
501 nearby  $\text{Sb}^{3+}$  ions to enable the redox exchange reactions, which effectively reduces the  
502 number of  $\text{Sb}^{4+}$  ions in the network. This explains why the highest EPR intensity of  $\text{Sb}^{4+}$ -ions  
503 was observed for the lowest  $\text{Sb}_2\text{O}_3$  content (Sb0.5) sample.

504 Offering different results, to a degree, were the X-ray irradiated glasses. The lab-scale  
505 XRF tube used for X-ray irradiations in the present study is a continuous source of X-rays,  
506 with photons of energy up to 35 keV. This X-ray energy is well below 1.02 MeV and hence  
507 inadequate for pair-production to generate electron ( $e^-$ ) and positron/hole ( $h^+$ ) pairs. Hence,  
508 the lack of holes ( $h^+$ ) from the X-ray irradiated samples prevented execution of the  $\text{Sb}^{3+} + h^+$   
509  $\rightarrow \text{Sb}^{4+}$  redox reaction. This explains why the EPR spectra of X-ray irradiated samples did  
510 not reveal the formation of  $\text{Sb}^{4+}$  ions in the X-ray irradiated glass network (Figure 5).

511 The optical absorption spectra of  $\text{Sb}_2\text{O}_3$ -modified SLS glasses reveal the non-obvious  
512 formation of radiation-induced colour centres at UV and visible wavelengths. This implies  
513 that the addition of  $\text{Sb}_2\text{O}_3$  to the SLS network reduced the possibility of  $HC_1$  and  $HC_2$  type of  
514 defect centre formation. The  $\text{Sb}^{3+}$ -ions in the glass network play the role of hole-trapping  
515 centres. The nearest Si-ion captures the electron ( $e^-$ ) that gives rise to the  $E^-$ -polaron in the  
516 network. Now, the electrons captured in the  $E^-$ -polaron must be absorbed by the  $\text{Sb}^{5+}$  ions to  
517 recover  $\text{Sb}^{3+}$ . As a result, the EPR spectra have shown a steady decrease of response intensity  
518 with  $\text{Sb}_2\text{O}_3$ -concentration in the glass network for various doses of  $\gamma$ -rays.

519

## 520 **5. Conclusions**

521 Laboratory simulant float glasses modified with  $\text{Sb}_2\text{O}_3$  has been studied for their high-  
522 energy ionising radiation performance. The radiation-resistant performance of these glasses  
523 was confirmed by irradiating with multiple doses (0.2, 2.0, and 5.0 MGy) of  $\gamma$ -rays ( $^{60}\text{Co}$   
524 nucleus decay) as well as with X-rays. The interaction of ionizing radiation with the undoped  
525 base glass (i.e., SLS) caused the formation of hole-centres ( $HC_1$  and  $HC_2$ ) and electron-  
526 centres ( $E'$  and  $E^-$ ), which produce strong, dark visible colouration. The increase of  $\text{Sb}_2\text{O}_3$   
527 concentration steadily reduces the formation of radiation-induced defects. As a result, this  
528 continuously reduces the radiation-induced colouration effects of the float glass. EPR spectra  
529 confirm that  $\text{Sb}^{3+}$ -ions are acting as hole-trapping centres to interact with the holes  
530 originating from the pair-production of  $\gamma$ -rays through the redox reaction of  $\text{Sb}^{3+} + h^+ \rightarrow$   
531  $\text{Sb}^{4+}$ . However, the X-rays have lower energy than  $\gamma$ -rays, which prevents the creation of  
532  $\text{Sb}^{4+}$ -ions. Notably, the Sb0.5 sample (0.5 mol%  $\text{Sb}_2\text{O}_3$ ) shows the optimum EPR response  
533 for  $\text{Sb}^{4+}$ -ions, which can be explained by ion-ion separation. Moreover, the introduction of  
534  $\text{Sb}^{3+}$ -ions in the network significantly reduced the ionizing radiation-induced defect-centres  
535 (e.g.,  $HC_1$ ,  $HC_2$ ,  $E'$  and  $E^-$ ) for the Sb0.5 sample. This significant reduction of ionizing  
536 radiation-induced colour centres has greatly improved the transparency of  $\text{Sb}_2\text{O}_3$ -modified  
537 float glass. The  $\text{Sb}^{3+}$  ions in the float glass network are working as hole-trapping centres,  
538 which confirms their radiation-resistant behaviour. Study of radiation resistance of float glass  
539 doped with lower concentrations of  $\text{Sb}_2\text{O}_3$  (i.e., lower than 0.5 mol%) is currently underway.  
540 This will enable optimal concentrations of  $\text{Sb}_2\text{O}_3$  to provide the greatest radiation resistance  
541 for the minimum Sb additions to be identified. In short, this study confirms the addition of  
542  $\text{Sb}_2\text{O}_3$  in the low-cost float-type soda-lime-silica glass proves beneficial in enabling the  
543 radiation-resistance behaviour that retains its transparency under an ionizing radiation  
544 environment. Therefore,  $\text{Sb}_2\text{O}_3$ -modified float glass is a more radiation-resistant type of float

545 glass that could potentially be applied in nuclear industries, consumer electronics, and other  
546 extreme environments.

547

548

549 **Acknowledgements:**

550 GG, T-YC and PAB acknowledge with thanks funding support from the UK Engineering and  
551 Physical Science Research Council (EPSRC) under Grant EP/R020957/1, New Industrial  
552 Systems: Manufacturing Immortality.

553

554 **References:**

555 [1] A. Bishay, Radiation induced color centers in multicomponent glasses, *J. Non. Cryst.*  
556 *Solids.* 3 (1970) 54–114.

557 [2] A. Bishay, I. Gomaa, Gamma-induced absorption in silicate glasses containing  
558 titanium, *Phys. Chem. Glasses* 9 (1968) 193–199.

559 [3] D.L. Griscom, E.J. Friebele, K.J. Long, J.W. Fleming, Fundamental defect centers in  
560 glass: electron spin resonance and optical absorption studies of irradiated phosphorus -  
561 doped silica glass and optical fibers, *J. Appl. Phys.* 54 (1983) 3743–3762.

562 [4] D. Möncke, D. Ehrt, Irradiation induced defects in glasses resulting in the  
563 photoionization of polyvalent dopants, *Opt. Mater. (Amst).* 25 (2004) 425–437.

564 [5] D. Möncke, D. Ehrt, Photoionization of As, Sb, Sn, and Pb in metaphosphate glasses,  
565 *J. Non. Cryst. Solids.* 345 (2004) 319–322.

566 [6] D. Möncke, D. Ehrt, Photoinduced redox-reactions and transmission changes in

- 567 glasses doped with 4d-and 5d-ions, *J. Non. Cryst. Solids.* 352 (2006) 2631–2636.
- 568 [7] D. Moncke, D. Ehrt, Photoionization of polyvalent ions, Nova Science Publishers,  
569 2010.
- 570 [8] S. Baccaro, A. Cecilia, E. Mihokova, M. Nikl, K. Nitsch, P. Polato, G. Zanella, R.  
571 Zannoni, Radiation damage induced by  $\gamma$  irradiation on  $\text{Ce}^{3+}$  doped phosphate and  
572 silicate scintillating glasses, *Nucl. Instruments Methods Phys. Res. Sect. A Accel.*  
573 *Spectrometers, Detect. Assoc. Equip.* 476 (2002) 785–789.
- 574 [9] S. Baccaro, A. Cemmi, I. Di Sarcina, F. Menchini, Gamma rays effects on the optical  
575 properties of Cerium-doped glasses, *Int. J. Appl. Glas. Sci.* 6 (2015) 295–301.
- 576 [10] D.L. Griscom, M. Mizuguchi, Determination of the visible range optical absorption  
577 spectrum of peroxy radicals in gamma-irradiated fused silica, *J. Non. Cryst. Solids.*  
578 239 (1998) 66–77.
- 579 [11] D.L. Griscom, Optical properties and structure of defects in silica glass, *J. Ceram. Soc.*  
580 *Japan.* 99 (1991) 923–942.
- 581 [12] D.L. Griscom, Self-trapped holes in amorphous silicon dioxide, *Phys. Rev. B.* 40  
582 (1989) 4224.
- 583 [13] D.L. Griscom, Self-trapped holes in pure-silica glass: A history of their discovery and  
584 characterization and an example of their critical significance to industry, *J. Non. Cryst.*  
585 *Solids.* 352 (2006) 2601–2617.
- 586 [14] H.-S. Tsai, D.-S. Chao, Y.-H. Wu, Y.-T. He, Y.-L. Chueh, J.-H. Liang, Spectroscopic  
587 investigation of gamma radiation-induced coloration in silicate glass for nuclear  
588 applications, *J. Nucl. Mater.* 453 (2014) 233–238.
- 589 [15] R.A. Weeks, Paramagnetic resonance of lattice defects in irradiated quartz, *J. Appl.*

- 590 Phys. 27 (1956) 1376–1381.
- 591 [16] M. Stapelbroek, D.L. Griscom, E.J. Friebele, G.H. Sigel Jr, Oxygen-associated  
592 trapped-hole centers in high-purity fused silicas, *J. Non. Cryst. Solids.* 32 (1979) 313–  
593 326.
- 594 [17] E.J. Friebele, D.L. Griscom, M. Stapelbroek and RA Weeks, Fundamental defect  
595 centers in glass: the peroxy radical in irradiated, high-purity, fused silica, *Phys. Rev.*  
596 *Lett.* 42 (1979) 1346.
- 597 [18] D.L. Griscom, Electron spin resonance characterization of self-trapped holes in  
598 amorphous silicon dioxide, *J. Non. Cryst. Solids.* 149 (1992) 137–160.
- 599 [19] D.L. Griscom, A minireview of the natures of radiation-induced point defects in pure  
600 and doped silica glasses and their visible/near-IR absorption bands, with emphasis on  
601 self-trapped holes and how they can be controlled, *Phys. Res. Int.* 2013 (2013).
- 602 [20] A.F. Zatsepin, V.B. Guseva, V.A. Vazhenin, M.Y. Artoymov, Paramagnetic defects in  
603 gamma-irradiated Na/K-silicate glasses, *Phys. Solid State.* 54 (2012) 1776–1784.
- 604 [21] K. Kadono, N. Itakura, T. Akai, M. Yamashita, T. Yazawa, Effects of iron on the  
605 formation and annihilation of X-ray irradiation induced non-bridging oxygen hole  
606 centers in soda-lime silicate glass, *J. Non. Cryst. Solids.* 356 (2010) 232–235.
- 607 [22] T. Maekawa, N. Murai, K. Haino, T. Yokokawa, The Structure and Thermal Stability  
608 of the Defect Center Induced in Irradiated Silicate Glasses, *J. Ceram. Soc. Japan.* 97  
609 (1989) 385–391.
- 610 [23] K. Kadono, N. Itakura, T. Akai, M. Yamashita, T. Yazawa, Formation of color centers  
611 in a soda-lime silicate glass by excimer laser irradiation, *J. Phys. Condens. Matter.* 22  
612 (2010) 45901.

- 613 [24] J.S. Stroud, Color centers in a cerium-containing silicate glass, *J. Chem. Phys.* 37  
614 (1962) 836–841.
- 615 [25] J.S. Stroud, Photoionization of  $Ce^{3+}$  in glass, *J. Chem. Phys.* 35 (1961) 844–850.
- 616 [26] J.S. Stroud, J.W.H. Schreurs, R.F. Tucker, Charge trapping and the electronic structure  
617 of glass, in: 7th Int. Congr. Glas., 1965.
- 618 [27] R.F. Tucker, Advances in glass technology, in: VIth Int. Congr. Glas., 1962.
- 619 [28] J.H. Mackey, H.L. Smith, J. Nahum, Competitive trapping in sodium disilicate glasses  
620 doped with  $Eu^{+3}$ , *J. Phys. Chem. Solids.* 27 (1966) 1773–1782.
- 621 [29] H.L. Smith, A.J. Cohen, Color Centers in X-Irradiated Soda-Silica Glasses, *J. Am.*  
622 *Ceram. Soc.* 47 (1964) 564–570.
- 623 [30] T.D. Henson, G.K. Torrington, Space radiation testing of radiation-resistant glasses  
624 and crystals, in: *Inorg. Opt. Mater.* III, 2001: pp. 54–65.
- 625 [31] G.A. Haynes, Effect of radiation on cerium-doped solar-cell cover glass, National  
626 Aeronautics and Space Administration, 1970.
- 627 [32] F.U. Xinjie, S. Lixin, L.I. Jiacheng, Radiation induced color centers in cerium -doped  
628 and cerium-free multicomponent silicate glasses, *J. Rare Earths.* 32 (2014) 1037–1042.
- 629 [33] J.E. Shelby, Introduction to glass science and technology, Royal Society of Chemistry,  
630 2007.
- 631 [34] H. Keppler, Crystal field spectra and geochemistry of transition metal ions in silicate  
632 melts and glasses, *Am. Mineral.* 77 (1992) 62–75.
- 633 [35] T. Bates, Ligand field theory and absorption spectra of transition-metal ions in glasses,  
634 *Mod. Asp. Vitr. State.* 2 (1962) 195–254.

- 635 [36] T. Brennan, J.C. Knight, G.A. Saunders, Fluorescence and absorption spectra of rare  
636 earth metaphosphate glasses, *Phys. Chem. Glas.* 40 (1999) 113–121.
- 637 [37] M. Yamane, Y. Asahara, *Glasses for photonics*, Cambridge University Press, 2000.
- 638 [38] X. Meng, S. Murai, K. Fujita, K. Tanaka, Intense visible emissions from  $d^0$  ions-doped  
639 silicate glasses, *J. Ceram. Soc. Japan.* 116 (2008) 1147–1149.
- 640 [39] B.L. Allsopp, G. Christopoulou, A. Brookfield, S.D. Forder, P.A. Bingham, Optical  
641 and structural properties of  $d^0$  ion-doped silicate glasses for photovoltaic applications,  
642 *Phys. Chem. Glas. J. Glas. Sci. Technol. Part B.* 59 (2018) 193–202.
- 643 [40] W.A. Weyl, *Coloured Glasses*, Society of Glass Technology, Sheffield, UK. 329  
644 (1951).
- 645 [41] M.H. Imanieh, B. Eftekhari Yekta, V. Marghussian, Effect of Ce, Sb, and Sn on  
646 solarization and crystallization of an X-ray-irradiated photosensitive glass, *Int. J. Appl.*  
647 *Ceram. Technol.* 7 (2010) 104–110.
- 648 [42] C.J. Magon, J.P.D. Gonzalez, J.F. Lima, H. Eckert, E.D. Zanotto, J. Lumeau, L.  
649 Glebova, L. Glebov, Electron Paramagnetic Resonance (EPR) studies on the photo-  
650 thermo ionization process of photo-thermo-refractive glasses, *J. Non. Cryst. Solids.*  
651 452 (2016) 320–324.
- 652 [43] D. Chia, B. Caudle, G.R. Atkins, M.P. Brungs, Effect of polyvalent ion additions on  
653 the solarisation of annealed and toughened glass, *Glas. Technol.* 41 (2000) 165–168.
- 654 [44] B.T. Long, L.J. Peters, H.D. Schreiber, Solarization of soda-lime-silicate glass  
655 containing manganese, *J. Non. Cryst. Solids.* 239 (1998) 126–130.
- 656 [45] H. Hosono, Y. Abe, H. Kawazoe, H. Imagawa, Solarization mechanism of glass  
657 containing  $Ce^{3+}$  and  $As^{5+}$ , *J. Non. Cryst. Solids.* 63 (1984) 357–363.

- 658 [46] H. Hosono, Y. Abe, Properties and mechanism of solarization in As-doped soda-lime-  
659 silica glasses with ultraviolet radiation, *J. Non. Cryst. Solids*. 125 (1990) 98–106.
- 660 [47] J.F. White, W.B. Silverman, Some studies on the solarization of glass, *J. Am. Ceram.*  
661 *Soc.* 33 (1950) 252–257.
- 662 [48] P.A. Bingham, C.M. Jackson, Roman blue-green bottle glass: chemical-optical  
663 analysis and high temperature viscosity modelling, *J. Archaeol. Sci.* 35 (2008) 302–  
664 309.
- 665 [49] K. Ouannes, K. Lebbou, B.-M. Walsh, M. Poulain, G. Alombert-Goget, Y. Guyot,  
666 New Er<sup>3+</sup> doped antimony oxide based glasses: Thermal analysis, structural and  
667 spectral properties, *J. Alloys Compd.* 649 (2015) 564–572.
- 668 [50] K. Ouannes, K. Lebbou, B.M. Walsh, M. Poulain, G. Alombert-Goget, Y. Guyot,  
669 Antimony oxide based glasses, novel laser materials, *Opt. Mater. (Amst)*. 65 (2017) 8–  
670 14.
- 671 [51] T. Som, B. Karmakar, Green and red fluorescence upconversion in neodymium-doped  
672 low phonon antimony glasses, *J. Alloys Compd.* 476 (2009) 383–389.
- 673 [52] Q. He, P. Wang, M. Sun, M. Lu, B. Peng, Significant improvement of gamma  
674 radiation resistance in CeO<sub>2</sub> doped phosphate glass by co-doping with Sb<sub>2</sub>O<sub>3</sub>, *Opt.*  
675 *Mater. Express*. 7 (2017) 1113–1121.
- 676 [53] G. Qian, S. Baccaro, A. Guerra, L. Xiaoluan, Y. Shuanglong, G. Iurlaro, G. Chen,  
677 Gamma irradiation effects on ZnO-based scintillating glasses containing CeO<sub>2</sub> and/or  
678 TiO<sub>2</sub>, *Nucl. Instruments Methods Phys. Res. Sect. B Beam Interact. with Mater.*  
679 *Atoms*. 262 (2007) 276–280.
- 680 [54] Z. Zhang, S. Baccaro, A. Cemmi, W. Shen, G. Chen, Effects of CuO co-doping on  $\gamma$ -

- 681 ray irradiation resistance of active ions doped phosphate glasses, Nucl. Instruments  
682 Methods Phys. Res. Sect. B Beam Interact. with Mater. Atoms. 311 (2013) 47–52.
- 683 [55] Y.M. Hamdy, F.H. ElBatal, F.M. Ezz-Eldin, H.A. ElBatal, Gamma rays interactions  
684 with transition metal doped-soda lime phosphate glasses evaluated by collective  
685 optical, FTIR spectral measurements, Silicon. 11 (2019) 673–684.
- 686 [56] F.H. El Batal, S.M.A. Naf, Spectroscopic studies of gamma-irradiated transition  
687 metals-doped soda lime phosphate glass, (2005).
- 688 [57] M. Yamashita, Z. Yao, Y. Matsumoto, Y. Utagawa, K. Kadono, T. Yazawa, X-ray  
689 irradiation-induced coloration of manganese in soda-lime silicate glass, J. Non. Cryst.  
690 Solids. 333 (2004) 37–43.
- 691 [58] J.H. Mackey, J. Nahum, spectral study of interconversion of  $\text{Eu}^{2+}$  and  $\text{Eu}^{3+}$  in silicate  
692 glasses, Phys. Chem. Glas. 9 (1968) 52.
- 693 [59] G. Jagannath, B. Eraiah, A. Gaddam, H. Fernandes, D. Brazete, K. Jayanthi, K.N.  
694 Krishnakanth, S. Venugopal Rao, J.M.F. Ferreira, K. Annapurna, A. R. Allu,  
695 Structural and femtosecond third-order nonlinear optical properties of sodium borate  
696 oxide glasses: effect of antimony, J. Phys. Chem. C. 123 (2019) 5591–5602.
- 697 [60] X. Heng, Q. Qian, X. Chen, L. Liu, X. Zhao, D. Chen, Z. Yang, Reduced radiation  
698 damage in a multicomponent phosphate glass by  $\text{Nb}^{5+}$  or  $\text{Sb}^{3+}$  doping, Opt. Mater.  
699 Express. 5 (2015) 2272–2280.
- 700 [61] E.J. Friebele, Radiation Effects on Glass, Pergamon Press Ltd, Encycl. Mater. Sci.  
701 Eng. 6 (1986).
- 702 [62] H.A. ElBatal, M.Y. Hassaan, M.A. Fanny, M.M. Ibrahim, Optical and FT infrared  
703 absorption spectra of soda lime silicate glasses containing nano  $\text{Fe}_2\text{O}_3$  and effects of

- 704 gamma irradiation, *Silicon*. 9 (2017) 511–517.
- 705 [63] M. Mohapatra, R.M. Kadam, R.K. Mishra, C.P. Kaushik, B.S. Tomar, S. V Godbole,  
706 Gamma Radiation-Induced Changes in Trombay Nuclear Waste Glass Containing  
707 Iron, *Int. J. Appl. Glas. Sci.* 4 (2013) 53–60.
- 708 [64] O.J. McGann, P.A. Bingham, R.J. Hand, A.S. Gandy, M. Kavčič, M. Žitnik, K. Bučar,  
709 R. Edge, N.C. Hyatt, The effects of  $\gamma$ -radiation on model vitreous wastefoms intended  
710 for the disposal of intermediate and high level radioactive wastes in the United  
711 Kingdom, *J. Nucl. Mater.* 429 (2012) 353–367.
- 712 [65] F.H. ElBatal, M.A. Ouis, R.M. Morsi, S.Y. Marzouk, Interactions of gamma rays with  
713 undoped and Mn-doped sodium phosphate glasses, *Philos. Mag.* 90 (2010) 2905–2924.
- 714 [66] H.D. Schreiber, N.R. Wilk Jr, C.W. Schreiber, A comprehensive electromotive force  
715 series of redox couples in soda-lime-silicate glass, *J. Non. Cryst. Solids.* 253 (1999)  
716 68–75.
- 717 [67] H.D. Schreiber, Redox processes in glass-forming melts, *J. Non. Cryst. Solids.* 84  
718 (1986) 129–141.
- 719 [68] A.M. Zoufakar, A.M. Abdel-Ghany, T.Z. Abou-Elnasr, A.G. Mostafa, S.M. Salem,  
720 H.H. El-Bahnaswy, Effect of antimony-oxide on the shielding properties of some  
721 sodium-boro-silicate glasses, *Appl. Radiat. Isot.* 127 (2017) 269–274.
- 722 [69] D.F. Franco, E.E. Carvajal, J.P. Donoso, M.A.P. Silva, A.C. Sant’Ana, H. Fares, C.J.  
723 Magon, M. Nalin, Structural and EPR studies of  $\text{Cu}^{2+}$  ions in  $\text{NaPO}_3\text{-Sb}_2\text{O}_3\text{-CuO}$   
724 glasses, *J. Non. Cryst. Solids.* 503 (2019) 169–175.
- 725 [70] S.Y. Marzouk, F.H. Elbatal, Infrared and UV-visible spectroscopic studies of gamma-  
726 irradiated  $\text{Sb}_2\text{O}_3\text{-B}_2\text{O}_3$  glasses, *J. Mol. Struct.* 1063 (2014) 328–335.

- 727 [71] R.R. Rakhimov, V.J. Turney, D.E. Jones, S.N. Dobryakov, Y.A. Borisov, A.I.  
728 Prokof'ev, A.I. Aleksandrov, Electron paramagnetic resonance and quantum-  
729 mechanical analysis of binuclear niobium clusters in lithium-niobium phosphate  
730 glasses, *J. Chem. Phys.* 118 (2003) 6017–6021.
- 731 [72] R. V Yusupov, I.N. Gracheva, A.A. Rodionov, P.P. Synchronov, A.I. Gubaev, A.  
732 Dejneka, L. Jastrabik, V.A. Trepakov, M.K. Salakhov, Experimental manifestations of  
733 the Nb<sup>4+</sup>-O<sup>-</sup> polaronic excitons in KTa<sub>0.988</sub>Nb<sub>0.012</sub>O<sub>3</sub>, *Phys. Rev. B.* 84 (2011) 174118.
- 734 [73] A.I. Aleksandrov, N.N. Bubnov, A.I. Prokof'ev, Stabilization of elements in unusual  
735 oxidation states and temperature-reversible dynamics of electron pairs in oxide glasses.  
736 EPR-investigation, *Appl. Magn. Reson.* 9 (1995) 251–266.
- 737 [74] T.-Y. Chen, P. Rautiyal, S. Vaishnav, G. Gupta, H. Schlegl, R.J. Dawson, A.W. Evans,  
738 S. Kamali, J.A. Johnson, C.E. Johnson, others, Composition-structure-property effects  
739 of antimony in soda-lime-silica glasses, *J. Non. Cryst. Solids.* (2020) 120184.
- 740 [75] L. Leay, W. Bower, G. Horne, P. Wady, A. Baidak, M. Pottinger, M. Nancekievill,  
741 A.D. Smith, S. Watson, P.R. Green, B. Lennox, J.A. LaVerne, S.M. Pimblott,  
742 Development of irradiation capabilities to address the challenges of the nuclear  
743 industry, *Nucl. Instruments Methods Phys. Res. Sect. B Beam Interact. with Mater.*  
744 *Atoms.* 343 (2015) 62–69.
- 745 [76] P. Rautiyal, G. Gupta, R. Edge, L. Leay, A. Daubney, M.K. Patel, A.H. Jones, P.A.  
746 Bingham, Gamma irradiation-induced defects in borosilicate glasses for high-level  
747 radioactive waste immobilisation, *J. Nucl. Mater.* 544 (2021) 152702.
- 748 [77] N.F. Mott, E.A. Davis, *Electronic processes in non-crystalline materials*, Oxford  
749 university press, 2012.

- 750 [78] R.K. Singh, A. Srinivasan, EPR and magnetic susceptibility studies of iron ions in  
751 ZnO-Fe<sub>2</sub>O<sub>3</sub>-SiO<sub>2</sub>-CaO-P<sub>2</sub>O<sub>5</sub>-Na<sub>2</sub>O glasses, *J. Magn. Magn. Mater.* 322 (2010) 2018–  
752 2022.
- 753 [79] V. Vercamer, Spectroscopic and Structural Properties of Iron in Silicate Glasses, PhD  
754 thesis, Université Pierre et Marie Curie-Paris VI, 2016.
- 755 [80] J.W.H. Schreurs, D.H. Davis, EPR spectrum of Sb<sup>4+</sup> in a silicate glass, *J. Chem. Phys.*  
756 71 (1979) 557–559.
- 757 [81] L. Skuja, Optically active oxygen-deficiency-related centers in amorphous silicon  
758 dioxide, *J. Non. Cryst. Solids.* 239 (1998) 16–48.
- 759 [82] J.H. Mackey, H.L. Smith, A. Halperin, Optical studies in X-irradiated high purity  
760 sodium silicate glasses, *J. Phys. Chem. Solids.* 27 (1966) 1759–1772.
- 761 [83] P.A. Bingham, J.M. Parker, T. Searle, J.M. Williams, I. Smith, Novel structural  
762 behaviour of iron in alkali-alkaline-earth-silica glasses, *Comptes Rendus Chim.* 5  
763 (2002) 787–796.
- 764 [84] P.A. Bingham, J.M. Parker, T.M. Searle, I. Smith, Local structure and medium range  
765 ordering of tetrahedrally coordinated Fe<sup>3+</sup> ions in alkali-alkaline earth-silica glasses, *J.*  
766 *Non. Cryst. Solids.* 353 (2007) 2479–2494.
- 767 [85] C. Ades, T. Toganidis, J.P. Traverse, High temperature optical spectra of soda-lime-  
768 silica glasses and modelization in view of energetic applications, *J. Non. Cryst. Solids.*  
769 125 (1990) 272–279.
- 770 [86] S. Xu, S. Zou, Y. Han, T. Zhang, Y. Qu, Obtaining High-Dose-Rate  $\gamma$ -Ray Detection  
771 With Commercial Off-the-Shelf CMOS Pixel Sensor Module, *IEEE Sens. J.* 19 (2019)  
772 6729–6735.

- 773 [87] B. Çaliskan, A.C. Çaliskan, Interaction with Matter of Ionizing Radiation and  
774 Radiation Damages (Radicals), Chapter 7 in: Ionizing Radiation Effects and  
775 Applications, edited by Boualem Djeddar, InTechOpen Publ., (2018) 135.
- 776 [88] D.W. Moon, J.M. Aitken, R.K. MacCrone, G.S. Cieloszyk, Phys. Chem. Glasses 16  
777 (1975) 91-102.
- 778 [89] P. A. Bingham, The environment of iron in silicate glasses, PhD thesis, University of  
779 Sheffield, UK, 2000.
- 780 [90] S.K. Mendiratta, E.G. De Sousa, Clustering and  $g=4.3$  ESR peak in iron-containing  
781 glasses, J. Mat. Sci. Lett. 7 (1988) 733.